



**HAL**  
open science

## Direct numerical simulations of liquid-liquid dispersions in a SMX mixer under different inlet conditions

Juan Pablo Valdes, Lyes Kahouadji, Fuyue Liang, Seungwon Shin, Jalel Chergui, Damir Juric, Omar Matar

► **To cite this version:**

Juan Pablo Valdes, Lyes Kahouadji, Fuyue Liang, Seungwon Shin, Jalel Chergui, et al.. Direct numerical simulations of liquid-liquid dispersions in a SMX mixer under different inlet conditions. Chemical Engineering Journal, 2023, 462, pp.142248. 10.1016/j.cej.2023.142248 . hal-03803802

**HAL Id: hal-03803802**

**<https://hal.science/hal-03803802v1>**

Submitted on 6 Oct 2022

**HAL** is a multi-disciplinary open access archive for the deposit and dissemination of scientific research documents, whether they are published or not. The documents may come from teaching and research institutions in France or abroad, or from public or private research centers.

L'archive ouverte pluridisciplinaire **HAL**, est destinée au dépôt et à la diffusion de documents scientifiques de niveau recherche, publiés ou non, émanant des établissements d'enseignement et de recherche français ou étrangers, des laboratoires publics ou privés.

# Direct numerical simulations of liquid-liquid dispersions in a SMX mixer under different inlet conditions

Juan Pablo Valdes<sup>a</sup>, Lyes Kahouadji<sup>a</sup>, Fuyue Liang<sup>a</sup>, Seungwon Shin<sup>b</sup>, Jalel Chergui<sup>c</sup>, Damir Juric<sup>c,d</sup> and Omar K. Matar<sup>a</sup>

<sup>a</sup>Department of Chemical Engineering, Imperial College London, South Kensington Campus, London SW7 2AZ, United Kingdom

<sup>b</sup>Department of Mechanical and System Design Engineering, Hongik University, Seoul 04066, Republic of Korea

<sup>c</sup>Université Paris Saclay, Centre National de la Recherche Scientifique (CNRS), Laboratoire Interdisciplinaire des Sciences du Numérique (LISN), 91400 Orsay, France

<sup>d</sup>Department of Applied Mathematics and Theoretical Physics, University of Cambridge, Centre for Mathematical Sciences, Wilberforce Road, Cambridge CB3 0WA, United Kingdom

## ARTICLE INFO

### Keywords:

Static mixer  
Two-phase flow  
Droplet breakup  
Mixing  
DNS

## ABSTRACT

The internal dynamics of static mixers handling liquid-liquid flows have been comprehensively explored over the past decade. Although the effect of the inlet configuration is often overlooked, a few studies have suggested a relationship between the phases' initial set-up and the performance of the mixer in terms of the droplet size distribution (DSD). Accordingly, different dispersed phase morphologies at the inlet of a SMX static mixer have been tested and their effect on the overall dispersion performance of the mixer has been evaluated based on the DSD and growth of interfacial area. In particular, three representative scenarios are considered: 1) Isolated cases, where one and three individual droplets are injected, mimicking a controlled syringe injection; 2) Numerous variable-sized droplets, simulating a pre-mixed/dispersed inlet; and 3) Jet inlet, emulating a standard phase injection from a gear pump. In addition, this study provides novel insight into the underlying physics dictating droplet deformation and breakage in SMX mixers for industrially-relevant scenarios. This can be achieved thanks to the massively-parallel high-fidelity three-dimensional direct numerical simulations computed with a robust hybrid front-tracking/level-set algorithm, which provides a wealth of information on intricate interfacial dynamics; this information cannot be obtained with experimental or volume-averaged modelling techniques implemented in past studies.


## 1. Introduction

Liquid-liquid dispersions are of major practical interest since they can be extensively found in multiple industrial applications in the energy, manufacturing, pharmaceutical, cosmetics, and food sectors [Lobry et al., 2011, Theron and Sauze, 2011]. The properties and quality of the finished emulsion products, as well as the energetic requirements to process them, depend largely on the control exerted on the droplet size distribution (DSD) [Chabanon et al., 2017]. Conventionally, emulsions are manufactured using agitated vessels. However, these devices usually entail large space requirements, high capital and operational costs, and offer limited emulsification efficiency due to a non-uniform spatial distribution of the energy dissipation throughout the tank [Chabanon et al., 2017, Thakur et al., 2003]. To address these issues, many industries have instead adopted the use of static mixers to handle emulsion systems.

Static mixers essentially consist of an array of motionless inserts, arranged in a structured configuration, which are commonly installed in pipes or channels to promote chaotic mixing by dividing and redistributing the flow streamlines sequentially in directions transverse to the main flow [Ghanem et al., 2014, Thakur et al., 2003]. These mixers offer continuous operation with comparatively lower energetic expenditure but simultaneously grant a more intense ( $\sim 10$  to 200

times higher) and uniform energy dissipation distribution than that achieved by stirred tanks [Lebaz and Sheibat-Othman, 2019, Rama Rao et al., 2007, Theron et al., 2010]. The energy dissipation intensity can be directly manipulated through accessible parameters such as the flowrate, thus enabling a higher degree of control over the emulsification process and yielding a uniform and reproducible drop size distributions (DSDs) [Valdés et al., 2022]. In addition, previous studies have demonstrated that static mixers can generate similar DSDs to those obtained in agitated vessels with remarkably lower residence times (30,000 less in Theron et al. [2010] study) and comparatively lower shear rates [Fradette et al., 2007a].

Liquid-liquid static mixing has been comprehensively studied over the past couple of decades, testing a multitude of design and operational parameters and fluid properties. Nonetheless, very few studies have acknowledged the effect of the entrance conditions on the dispersion dynamics taking place and a standardized set-up has not been agreed on. Furthermore, very few studies have attempted to describe the underlying physics revolving around the dispersion process itself. One of the earliest studies comes from Grace [1982] who delved into the dispersion of high viscosity fluids, discussing in detail the droplet Sauter mean diameter ( $D_{32}$ ) behavior against a wide range of fluid properties and operational parameters. Grace [1982] was the first to analyze the effect of different dispersed phase inlet conditions on the  $D_{32}$  by testing two configurations: an unbroken jet and a drop

 j.valdes20@imperial.ac.uk (J.P. Valdes)  
ORCID(s): 0000-0003-3249-5194 (J.P. Valdes)

feed coming from a naturally broken jet, where it was generally noticed that lower droplet diameters were attained with the broken jet/drop feed. In spite of this, no further detail was given on the underlying physics involving the dispersed phase inlet morphology. To the best of the authors' knowledge, the only other early study that acknowledges some effect of the dispersed phase inlet configuration was that of Berkman and Calabrese [1988]. In this work, the outlet DSD was observed to depend on the initial DSD at high dispersed phase viscosities ( $\mu_d > 150\text{mPa} \cdot \text{s}$ ) and Reynolds numbers ( $Re$ ) in the range  $Re < 12,000$ . In contrast, the outlet DSD was concluded to be nearly independent of the inlet DSD at lower viscosities, regardless of  $Re$ . This was mostly attributed to the higher breakage events occurring as a result of lower stabilizing viscous forces inside the droplet [Berkman and Calabrese, 1988].

In recent years, researchers have largely concentrated on the DSD behavior and general flow dynamics within multi-layered static mixers, focusing specifically on the SMX family [Legrand et al., 2001, Das et al., 2005, Rama Rao et al., 2007, Gingras et al., 2007, Fradette et al., 2007b, Theron et al., 2010, Kiss et al., 2011, Theron and Sauze, 2011, Baumann et al., 2012, Das et al., 2013, Chabanon et al., 2017, Forte et al., 2019]. Similar to earlier works, different inlet configurations have been tested but little emphasis has been given to the underlying physics occurring due to alterations in the dispersed phase dynamics and morphology at the inlet. Instead, only the global effect of the dispersed phase fraction ( $\phi_d$ ) or the mixture's flowrate is usually discussed. Legrand et al. [2001] and Das et al. [2005] studied turbulent and laminar/transitional mixing of oil-in-water emulsions in a SMX, respectively, varying  $\phi_d$  through the same inlet configuration which consisted of pumping both phases into a T-junction located upstream from the mixing elements. These studies proposed semi-empirical porous media models for the  $D_{32}$  as a function of the global flowrate and the continuous phase properties, but neither model incorporated any relevant parameter concerning the dispersed phase.

A similar pre-mixed T-junction inlet configuration was used by Gingras et al. [2007], Theron et al. [2010], Theron and Sauze [2011] and Chabanon et al. [2017], but none of them accounted for inlet effects in the proposed correlations or in the measured DSDs. In fact, Chabanon et al. [2017] highlighted the possible effects of having different pre-mixed inlets (perpendicular T-junction or parallel injection as in Hirschberg et al. [2009]) and advised to verify the pre-emulsion DSD at the inlet to isolate pumping effects that may cause additional breakup. Moreover, Baumann et al. [2012] discussed a similar point, arguing that on-line pre-mixed inlets may strongly fluctuate as a function of the experimental conditions (e.g., flowrate), affecting the mixer's performance. For this reason, Baumann et al. [2012] implemented an off-line pre-mixing step in a stirred vessel, showing that similar drop sizes are obtained as in the on-line method but with less variability. Other inlet configurations such as Y-shape junction [Kiss et al., 2011], syringe/drop feed [Liu et al., 2005, Forte et al., 2019], and jet inlet [Rama Rao et al., 2007, Das

et al., 2013] have been employed as well.

Liu et al. [2005] is one of the very few to carry out a fundamental study on the droplet breakup mechanics in the SMX and recognize the effect of the inlet conditions on these mechanisms and on the maximum drop size ( $d_{max}$ ) at the outlet of the mixer. Liu et al. [2005] implemented a variable-sized drop feed inlet and observed that drops with a similar size to the crossbar gap were less likely to break than smaller ones, due to the location of high strain rate zones in between bars. Moreover, it was concluded that the outlet  $d_{max}$  became independent of the inlet droplet size at higher flowrates and that smaller droplets had less probability of colliding at the cross-points, thus leading to less breakage events. In contrast, Rama Rao et al. [2007] and Das et al. [2013] implemented two considerably different dispersed phase inlet configurations (central pipe injection below the continuous phase inlet and L-shaped injection above the continuous phase inlet), but no physical consideration was given to the different hydrodynamics spawning from these set-ups. Instead, only  $\phi_d$ , calculated from the phases flowrates, was taken into consideration when processing the DSD data.

Numerous computational studies have been carried out in this area as well, implementing several numerical frameworks such as two-phase Eulerian turbulent modelling through LES [Pianko-Oprych and Jaworski, 2009, 2010] and RANS approaches [Abdolkarimi and Ganji, 2014, Vasilev and Abiev, 2018a,b], Eulerian-Lagrangian [Haddadi et al., 2020], Lattice Boltzmann Method [Leclaire et al., 2020] and Population Balance Modelling (PBM) [Azizi and Taweel, 2011, Lebaz and Sheibat-Othman, 2019, Vikhansky, 2020]. Usually, these works engage in similar investigations as the experimental studies, providing further insights into the hydrodynamics and occasionally coupling Lagrangian particle tracking analysis or DSD estimations using PBM. Nonetheless, the reasoning behind selecting a given inlet configuration is usually dismissed, and the implications on the governing physical mechanisms is not addressed. This comes as a natural consequence for various numerical frameworks where it is not possible to provide detailed information of the interfacial dynamics between phases. Lebaz and Sheibat-Othman [2019] is the only study that directly addressed the influence of the inlet DSD through the use of a PBM model. Lebaz and Sheibat-Othman [2019] demonstrated that different inlet DSDs (determined by the residence time spent in the off-line pre-mixing step) indeed affected the outlet DSD even with a large number of elements ( $n_E > 8$ ), as opposed to the usual assumption that having enough mixing elements guaranteed an equilibrium state, thus rendering the outlet DSD independent from the inlet. Furthermore, Lebaz and Sheibat-Othman [2019] suggested that the steady state is highly dependent on the operational conditions and not only on the number of elements. Therefore, predictive models should account for the inlet DSD.

The state-of-the-art discussed in the foregoing exposes a gap in the fundamental understanding of static mixers dispersion dynamics. To the best of the authors' knowledge, very few studies have provided highly detailed data on the in-

tricacies surrounding such dynamics, particularly for different inlet set-ups. Although the inlet configuration has often been overlooked, multiple studies have agreed upon its relevance on the mixer’s performance in terms of DSD. Hence, this study seeks to implement a robust three-dimensional direct numerical simulation (DNS) approach coupled with high-fidelity interface capturing algorithms that is capable of providing a wealth of information on the underlying governing physics of such scenarios. The front-tracking technique [Shin et al., 2017, 2018] implemented in this study can handle all types of complex interfacial singularities, as has been extensively demonstrated in previous papers detailing similar physical mechanisms to the ones addressed in this study (i.e., ligament stretching and breakup [Constante-Amores et al., 2020], capillary instabilities of liquid threads [Constante-Amores et al., 2021]). The results provided in this paper will enable a physics-based evaluation of the SMX performance when subjected to three relevant operating scenarios in a laminar regime: 1. Isolated scenario: drop-feed injection, 2. Pre-mixed inlet: numerous variable-sized droplets and, 3. Jet inlet: standard phase injection from a gear pump.

## 2. Problem formulation

### 2.1. Geometry and Grid Considerations

The mixer considered in this study is a standard Sulzer SMX (multi-layer design), which essentially consists of an array of cross-bars forming a X-shaped lattice, where each bar is inclined by  $45^\circ$  against the pipe axis and the elements are rotated by  $90^\circ$  with respect to the adjacent element (see Figure 1) [Valdés et al., 2022]. The mixer configuration used for this work consists of a 2-element mixer with an entrance length of  $L_h = D_p$ . The initial  $L_h$  was determined from the well-known expression for laminar flow given by  $L_h = 0.05 Re D_p$  [Incropera et al., 2007], taking the largest  $Re$  tested in Liu et al. [2005]. After verifying a correct convergence of the inlet flow field in the single-phase validation, a smaller  $L_h$  was adopted for the remaining cases in order to reduce the computational cost whilst guaranteeing an appropriate flow development. The remaining geometrical features of the mixer considered herein are summarized in Table 1.

The mixer was built in a modular manner from primitive geometrical objects and basic operations using a static distance function  $\psi(x, y, z)$  that accounts for the interaction between the solid and the fluid phases (positive values for the fluid region and negative ones for the solid region) [Kahouadji et al., 2018]. The model shown in Figure 1 corresponds to an iso-value  $\psi(x, y, z) = 0$ . Further detail into the construction process carried out in this work can be found in Kahouadji et al. [2018].

The size of the computational domain for the simulations is  $0.064 \times 0.016 \times 0.016 \text{m}^3$ . This domain consists of a three-dimensional structured Cartesian grid, divided into  $12 \times 6 \times 6$  sub-domains. The Cartesian structured grid per sub-domain is split into a  $128 \times 64 \times 64$  configuration, rendering a global structured mesh of  $1536 \times 384 \times 384$ . This implies that cells will have an approximate volume of  $7.0 \times 10^{-14} \text{m}^3$  and hence

**Table 1**

Geometrical details for the mixer based on the specifications given by Liu et al. [2005]

Feature	
Pipe Diameter $D_p$ (m)	0.01575
Number of Crossbars	8
Length $L$ (m)	0.064
Aspect Ratio $L_E/D_p$	1
Bar Width $W$ (m)	0.00193
Bar Thickness $Th$ (m)	0.00102

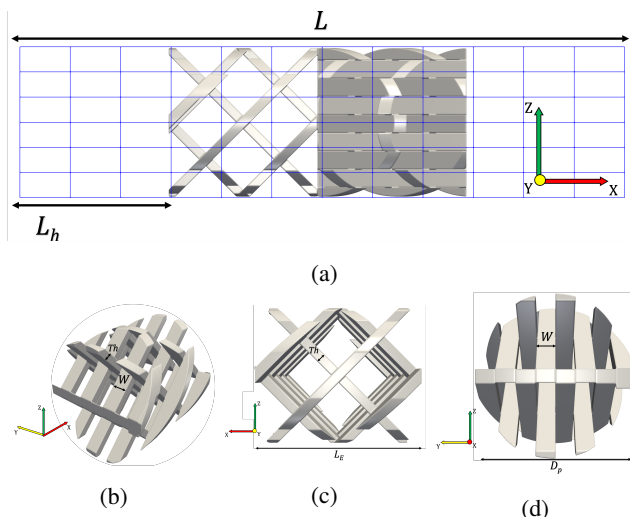


**Figure 1:** Computational domain built for the two phase cases, based on Liu et al. [2005] specifications. a) 2-Element longitudinal view and computational subdomains highlighted, b) Single element 3-D view, c) Cross-section view, and d) Longitudinal view.

an average size of  $4.12 \times 10^{-5} \text{m}$ . This resolution was devised to comfortably resolve the experimental droplet diameters reported by Liu et al. [2005] at the inlet, which are around 1 mm in size. The grid is therefore capable of capturing reliably the droplet’s deformation by providing roughly 24 cells per droplet diameter, which falls within the suggested range for interface-tracking methods [Andersson et al., 2011]. Furthermore, this set-up grants a sufficient resolution for the droplets and ligaments obtained during the dispersion process since the interface tracking algorithm implemented in this study (detailed in subsection 2.2) provides sub-grid resolution due to the nature of the hybrid Front-tracking/Level-set methodology employed. A grid independence test was carried out as well for the two-phase validation case considered, as discussed later in subsection 3.2, to further validate the mesh selected for the core simulations in this paper.

### 2.2. Numerical Methods

The numerical code solves the continuity and momentum governing equations for an incompressible flow, written below for a three-dimensional Cartesian domain  $\mathbf{x} = (x, y, z) \in [0, 0.064] \times [0, 0.016] \times [0, 0.016] \text{m}$  using a single-field for-

mulation:

$$\nabla \cdot \mathbf{u} = 0, \quad (1)$$

$$\rho \left( \frac{\partial \mathbf{u}}{\partial t} + \mathbf{u} \cdot \nabla \mathbf{u} \right) = -\nabla P + \rho \mathbf{g} + \nabla \cdot \mu (\nabla \mathbf{u} + \nabla \mathbf{u}^T) + \mathbf{F}, \quad (2)$$

where  $P$ ,  $\mathbf{u}$ ,  $\mathbf{g}$ , and  $\mathbf{F}$  denote pressure, velocity, gravity, and the local surface tension force at the interface. The density  $\rho$  and viscosity  $\mu$  are defined in the entire domain by:

$$\begin{aligned} \rho(\mathbf{x}, t) &= \rho_o + (\rho_w - \rho_o) \mathcal{H}(\mathbf{x}, t), \\ \mu(\mathbf{x}, t) &= \mu_o + (\mu_w - \mu_o) \mathcal{H}(\mathbf{x}, t). \end{aligned} \quad (3)$$

The indicator function  $\mathcal{H}(\mathbf{x}, t)$  stands for a numerical Heaviside function, generated through a vector distance function  $\varphi(\mathbf{x})$  computed directly from the tracked interface [Shin and Juric, 2009a].  $\mathcal{H}(\mathbf{x}, t)$  is defined as zero in the oil phase (denoted by subscript  $o$ ) and unity in the aqueous phase (denoted by subscript  $w$ ), and is resolved numerically with a sharp but smooth transition across 3 to 4 grid cells [Shin et al., 2017].

The surface tension force  $\mathbf{F}$  is implemented following the hybrid formulation proposed in [Shin et al., 2005, Shin and Juric, 2009a]:

$$\mathbf{F} = \sigma \kappa_H \nabla \mathcal{H}, \quad (4)$$

where  $\sigma$  is the surface tension coefficient, assumed to be a constant, and  $\kappa_H$  is twice the mean interface curvature field calculated on the Eulerian grid through Eqs. 5-7:

$$\kappa_H = \frac{\mathbf{F}_L \cdot \mathbf{N}}{\mathbf{N} \cdot \mathbf{N}}, \quad (5)$$

$$\mathbf{F}_L = \int_{\Gamma(t)} \kappa_f \mathbf{n}_f \delta(\mathbf{x} - \mathbf{x}_f) dS, \quad (6)$$

$$\mathbf{N} = \int_{\Gamma(t)} \mathbf{n}_f \delta(\mathbf{x} - \mathbf{x}_f) dS, \quad (7)$$

Here,  $\mathbf{x}_f$  is a parameterization of the interface,  $\Gamma(t)$ , and  $\delta(\mathbf{x} - \mathbf{x}_f)$  is the three-dimensional Dirac delta function which vanishes everywhere except at the interface, localised at  $\mathbf{x} = \mathbf{x}_f$ ;  $\mathbf{n}_f$  is the unit vector to the interface and  $dS$  is the infinitesimal area of the interface element;  $\kappa_f$  is twice the mean interface curvature, but in this expression it is obtained on the Lagrangian interface structure [Shin et al., 2017]. All geometrical elements ( $\mathbf{n}_f, dS$ ) in  $\mathbf{N}$  are computed directly from the Lagrangian grid and then distributed onto the Eulerian grid using a discrete delta function similar to the Immersed Boundary Method developed by Peskin [1977]. A detailed description of the calculations involving  $\mathbf{F}, \mathbf{N}$  and the indicator function  $\mathcal{H}$  can be found in the following references [Shin et al., 2005, Shin, 2007, Shin and Juric, 2007, 2009a,a,b, Shin et al., 2017].

The Lagrangian interface is advected by integrating Eq. 8 with a second-order Runge-Kutta method, where the interface velocity  $\mathbf{V}$  is interpolated from the Eulerian velocity,

$$\frac{d\mathbf{x}_f}{dt} = \mathbf{V}. \quad (8)$$

The numerical code structure consists essentially of two main modules: i) a module to solve the incompressible Navier-Stokes equations (Eq. 1,2) and ii) a module for the interface solution (Eq. 8), including a tracking of the phase front, initialization and reconstruction of the interface where necessary [Shin et al., 2017, Kahouadji et al., 2018]. An algebraic domain decomposition strategy is implemented for parallelization, where communication across processes is performed with Message Passing Interface (MPI) protocols.

For this work, the temporally discretized form of the momentum equation (see Eq. 2) can be written as follows,

$$\begin{aligned} \frac{\mathbf{u}^{n+1} - \mathbf{u}^n}{\Delta t} &= -(\mathbf{u} \cdot \nabla \mathbf{u})^n + \mathbf{g} \\ + \frac{1}{\rho^{n+1}} &\left( \nabla \cdot \mu^{n+1} (\nabla \mathbf{u} + \nabla \mathbf{u}^T)^{n+1} + \mathbf{F}^{n+1} - \nabla P^{n+1} \right), \end{aligned} \quad (9)$$

As detailed by Shin et al. [2017], Kahouadji et al. [2018], the Navier–Stokes solver calculates the velocity  $\mathbf{u}$  and pressure  $P$  variables on a fixed, uniform Eulerian grid employing Chorin’s projection method [Chorin, 1968] with incremental pressure correction [Goda, 1979]. The spatial discretization is performed using the well-known staggered mesh, MAC method [Harlow and Welch, 1965], which is a cell-centered Finite Difference scheme. All spatial derivatives are discretized using standard second-order centered differences [Shin et al., 2017]. However, the non-linear convection term in Eq. 9 is discretized with a second-order essentially non-oscillatory (ENO) method [Shu and Osher, 1989, Sussman et al., 1998]. Time integration is performed in two sub-steps, which includes a semi-implicit calculation of an intermediate unprojected velocity  $\tilde{\mathbf{u}}$  as displayed below in Eqs. 10 and 11:

$$\begin{aligned} \frac{\tilde{\mathbf{u}} - \mathbf{u}^n}{\Delta t} &= -(\mathbf{u} \cdot \nabla \mathbf{u})^n + \mathbf{g} \\ + \frac{1}{\rho^{n+1}} &\left( \nabla \cdot \mu^{n+1} (\nabla \tilde{\mathbf{u}} + \nabla \tilde{\mathbf{u}}^T) + \mathbf{F}^{n+1} - \nabla P^n \right), \end{aligned} \quad (10)$$

$$\frac{\mathbf{u}^{n+1} - \tilde{\mathbf{u}}}{\Delta t} = -\frac{1}{\rho^{n+1}} \nabla (P^{n+1} - P^n). \quad (11)$$

By enforcing  $\mathbf{u}^{n+1}$  to obey the divergence-free condition, the pressure increment can be computed by solving an elliptic Poisson equation:

$$\nabla \cdot \frac{1}{\rho^{n+1}} \nabla (P^{n+1} - P^n) = \frac{\nabla \cdot \tilde{\mathbf{u}}}{\Delta t}, \quad (12)$$

leaving the final expression for the updated velocity as:

$$\mathbf{u}^{n+1} = \tilde{\mathbf{u}} - \frac{\Delta t}{\rho^{n+1}} \nabla (P^{n+1} - P^n). \quad (13)$$

The linear solver used for the implicit viscous terms of the velocity field is the standard Generalized Minimal Residual (GMRES) method. A modified multigrid iterative method was utilized to solve the elliptic Poisson equation for the pressure increment. Further detail on the operation of these solvers can be found in [Shin et al., 2017, Kahouadji et al., 2018].

The temporal integration scheme for all simulations is based on a second-order GEAR method [Tucker, 2014], with implicit solution of the viscous terms of the velocity components. The time step  $\Delta t$  chosen at each temporal iteration is sought to fulfill an adaptive minimization criterion shown below:

$$\Delta t = \min \left\{ \Delta t_{cap}, \Delta t_{vis}, \Delta t_{CFL}, \Delta t_{int} \right\} \quad (14)$$

where  $\Delta t_{cap}$ ,  $\Delta t_{vis}$ ,  $\Delta t_{CFL}$ , and  $\Delta t_{int}$  represent the capillary, the viscous, the Courant-Friedrichs-Lewy (CFL), and interfacial CFL time steps, accordingly. Each criterion is defined by the following bounds:

$$\begin{aligned} \Delta t_{cap} &\equiv \frac{1}{2} \sqrt{\frac{(\rho_o + \rho_w) \Delta x_{\min}^3}{\pi \sigma}}, \\ \Delta t_{vis} &\equiv \left( \frac{\rho_o}{\mu_o} \right) \frac{\Delta x_{\min}^2}{6}, \\ \Delta t_{CFL} &\equiv \min_j \left( \min_{domain} \left( \frac{\Delta x_j}{u_j} \right) \right), \\ \Delta t_{int} &\equiv \min_j \left( \min_{\Gamma(t)} \left( \frac{\Delta x_j}{\|\mathbf{V}\|} \right) \right) \end{aligned} \quad (15)$$

where  $\Delta x_{\min} = \min_j(\Delta x_j)$  refers to the minimum size of a given cell  $j$ ,  $u_j$  and  $\mathbf{V}$  are the fluid and interface velocities, respectively.

### 2.3. Simulated cases

Following the discussion given earlier in Section 1, two common inlet configurations for the dispersed phase can be identified: 1) pre-mixed/pre-emulsified inlets coming either from a perpendicular injection (e.g., T-junction) or after a pre-mixing operation (e.g., stirrer located off or on-line), and 2) jet-type inlet, parallel to the continuous phase injection, usually coming from a conventional gear pump. Considering this, three scenarios with two case studies each will be tackled in this paper, as displayed below in Table 2. The first two rows (1 and 3 drops) correspond to a controlled injection or ‘isolated’ scenario, where the interface’s deformation, breakage and coalescence mechanisms can be thoroughly examined, providing a deeper understanding on the underlying governing physics. The 3<sup>rd</sup> and 4<sup>th</sup> row in Table 2 correspond to the pre-mixed scenario, simulating a coarse and fine dispersion that has been generated before entering the mixer. The final row refers to two jet-type simulations with a dispersed phase flow rate set to equal and half of the continuous phase flowrate.

The study conducted by Liu et al. [2005] will be taken as the benchmark to set-up the simulations performed herein. Hence, the properties of the fluids are defined as follows: continuous phase (aqueous solution) viscosity and density:  $\mu_c = 0.615 \text{ Pa} \cdot \text{s}$  and  $\rho_c = 1364 \text{ kg} \cdot \text{m}^{-3}$ , respectively; dispersed phase (silicon oil) viscosity and density:  $\mu_d = 0.0984 \text{ Pa} \cdot \text{s}$  and  $\rho_d = 960 \text{ kg} \cdot \text{m}^{-3}$ , respectively and a surface tension of  $\sigma = 0.036 \text{ N} \cdot \text{m}^{-1}$ . The single droplet simulation (baseline case) was directly copied from an experimental test reported in Liu et al. [2005]. Thus, the continuous phase flowrate ( $Q_c = 9.0 \times 10^{-6} \text{ m}^3 \text{ s}^{-1}$ ) was set to achieve a  $Re = 1.63$ , where  $Re = 4\rho_c Q_c / \pi D_p \mu_c$  and the initial drop diameter was set to  $D_0 = 1.660 \text{ mm}$ . The same continuous phase flowrate  $Q_c$  was used for all cases to ensure comparable results between the scenarios considered. The drop size distribution for the pre-mixed cases has been roughly based on experimental results reported in previous studies [Lebaz and Sheibat-Othman, 2019]. The gravity for all simulations was defined in the negative  $x$ -axis direction, following the specifications given by Liu et al. [2005]. All simulations were stopped as soon as the first droplet/segment of dispersed phase exited the domain in order to maintain consistency when discussing the evolution of the number of drops or the interfacial area.

### 3. Validation

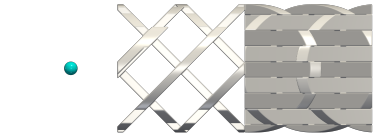
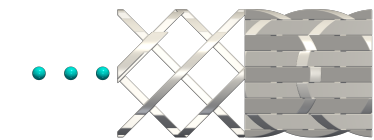



The numerical framework previously described has been thoroughly validated in fundamental applications related to the phenomena studied in this work (e.g., ligament stretching and breakup [Constante-Amores et al., 2020]). However, it is worth providing a validation for the novel, more applied area considered herein, namely full scale static mixing. For this, two cases have been envisioned: 1) single-phase hydrodynamic calculations based on experimental and computational results reported by Rama Rao et al. [2007] and Liu et al. [2005, 2006] to verify the validity of the geometrical model constructed; and 2) two-phase droplet deformation and breakup based on Liu et al. [2005] experimental and numerical results, to assess the accuracy of the grid resolution utilized. The single phase case considers a 6-element SMX mixer with the same characteristics given in Table 1, while the two-phase validation is ran in a single SMX element with a diameter of  $D_p = 0.03792 \text{ m}$  and a crossbar width  $W$  and thickness  $Th$  of 4.74 mm and 1.66 mm, respectively, based on a case study detailed in Liu et al. [2005], where the aim is to replicate the flow around the vicinity of the cross-point where the drop impacts.

#### 3.1. Single-Phase Validation: Hydrodynamics

Pressure calculations can be considered as an adequate criterion to evaluate the correctness of the velocity fields computed numerically, given their proneness to artificial oscillations and numerical error [Rauline et al., 1998]. Six cases are set with  $Re$  ranging from 4.14 to 28.05. The pressure drop results are shown in Figure 2a. A satisfactory agreement can be observed between the simulations and both the experimental data and the Ergun based model estimations

**Table 2**

Specifications of the different inlet conditions simulated throughout this work. Baseline case (1-Drop) is based on the experimental work by Liu et al. [2005]

Case	Setup	Specifications
1-Drop		$D_0 = 1.66 \text{ mm}$
3-Drops		3 drops with $D_0 = 1.66 \text{ mm}$
Coarse Pre-mix		160 drops with a size range between $0.4 < D_0(\text{mm}) < 2$
Fine Pre-mix		160 drops with a size range between $0.4 < D_0(\text{mm}) < 1.2$
Jet		Two flowrates ( $9 \times 10^{-6}$ and $3 \times 10^{-6} \text{ m}^3/\text{s}$ for the dispersed phase) with a constant inlet diameter of 4 mm

given in Rama Rao et al. [2007], with average deviations of 17.15% and 9.66%, respectively. The slightly larger deviation against experimental data can be attributed to the fact that the SMX geometry constructed herein does not follow exactly the guidelines given by Rama Rao et al. [2007]. The algorithm employed to build the SMX geometry can only handle one constant crossbar width and thickness, whilst the SMX detailed in Rama Rao et al. [2007] has larger  $W$  and  $Th$  close to the pipe wall. To guarantee the robustness of the results obtained for the SMX studied, additional flow field comparisons were performed against previous studies. For this, a case at  $Re = 0.35$  was set-up following one of Liu et al. [2005] cases, with the same continuous phase properties mentioned in subsection 2.3, to evaluate the correctness of the velocity and strain rate fields obtained. The strain rate is calculated from Eq. 16,

$$\dot{\gamma} = \sqrt{2(\mathbf{D} : \mathbf{D})}, \quad (16)$$

where  $\mathbf{D}$  stands for the rate of deformation tensor which is defined following Eq. 17:

$$\mathbf{D} = \frac{1}{2}(\nabla \mathbf{u} + (\nabla \mathbf{u})^T) \quad (17)$$

This tensor provides information on the rate of stretching and shearing that is present in the flow.

The strain rate contour and velocity streamlines depicted in Figure 2b are in full agreement with the CFD predictions

carried out by Liu et al. [2005] and Liu et al. [2006] in the commercial code FLUENT. In particular, the low velocity recirculation regions close to the bars, as well as the high velocity corridors formed in between crossbars, shown to the right of Figure 2b, closely resemble those depicted in Liu et al. [2006] work for a similar operational condition. Moreover, it can be noted that the maximum value of the projected velocity vector magnitude on the cross-section plane  $yz$  ( $\sqrt{u_z^2 + u_y^2}$ ), shown to the right in Figure 2b, lies within the same order of magnitude as the values reported by Liu et al. [2006] ( $\sqrt{u_z^2 + u_y^2} < 0.02$  for  $Re = 0.44$  in Liu et al. [2006] while the case considered herein computes  $\sqrt{u_z^2 + u_y^2} < 0.025$  for  $Re = 0.35$ ). Analogously, the location and magnitude of the characteristic strain regions generated close to the static inserts and in between crossbars, shown to the left of Figure 2b, are also physically consistent with the CFD results reported by both studies [Liu et al., 2005, 2006]. In particular, the distinctive strain rate slumps in the gaps between bars, immediately followed by high strain-rates in the vicinity of the bars can be confirmed. Moreover, the maximum strain rate in the vicinity of the bars was estimated to be  $\dot{\gamma} < 100\text{s}^{-1}$  as reported by Liu et al. [2005] at the same  $Re$  compared to  $\dot{\gamma} < 80\text{s}^{-1}$  in the present work. Similarly, the average strain rate values in the gaps between crossbars oscillates between  $\dot{\gamma} \sim 20 - 30\text{s}^{-1}$  for Liu et al. [2005] com-

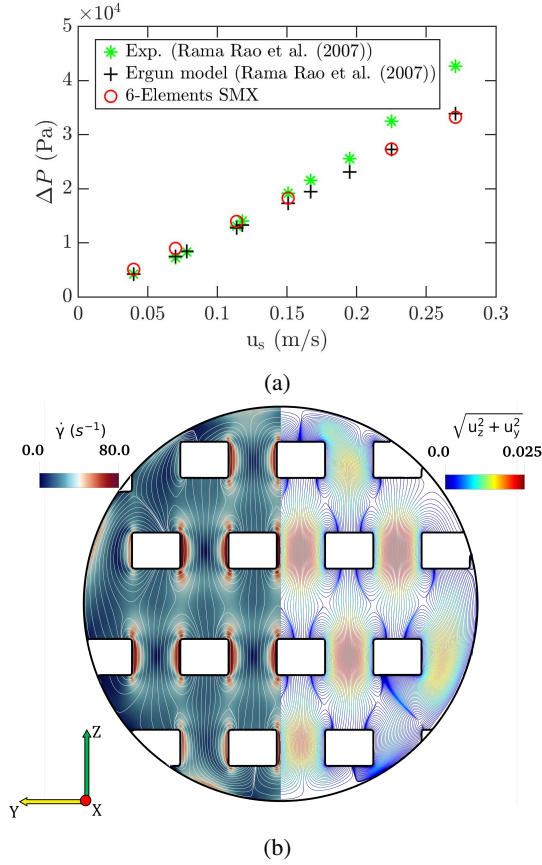


**Figure 2:** Single-phase validation results: a) Pressure drop calculations against Rama Rao et al. [2007], and b) Strain rate contour and projected velocity streamlines at  $Re = 0.35$ .

pared to  $\dot{\gamma} \sim 10 - 20s^{-1}$  in this study.

### 3.2. Two-Phase Validation: Laminar Droplet Breakup

The next step is to assess the accuracy of the interface capturing algorithm and the independence of the grid's resolution. For this, the 1-drop baseline case shown in Table 2 and an additional case based on Liu et al. [2005] experimental tests were considered. The physical properties of the fluids tested in the additional case differ slightly from those given in subsection 2.3, being  $\mu_c = 0.556Pa \cdot s$  and  $\rho_c = 1364kg \cdot m^{-3}$  for the continuous phase and  $\mu_d = 0.49Pa \cdot s$  and  $\rho_d = 970kg \cdot m^{-3}$  for the dispersed phase [Liu et al., 2005].

Firstly, the hydrodynamics associated with the droplet deformation mechanism can be evaluated by computing the maximum instantaneous stretching efficiency  $e_{\lambda,max}$  profile, which is calculated from the expression given in Eq. 18 as detailed by Liu et al. [2005, 2006].

$$e_{\lambda,max} = \frac{\lambda_1}{(\mathbf{D} : \mathbf{D})^{1/2}} \quad (18)$$

Here,  $\lambda_1$  is the largest eigenvalue of  $\mathbf{D}$ , which represents the maximum specific rate of length stretch determined by  $D \ln \lambda / Dt$ , when the line orientation follows the respective

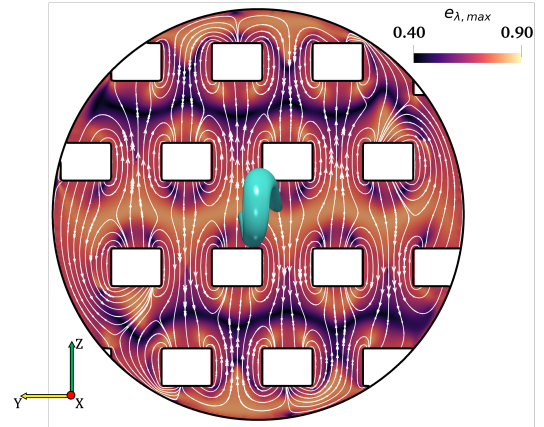


**Figure 3:** Velocity streamlines and maximum stretching efficiency contour at  $Re = 1.63$  for the 1-drop case.  $yz$ -slice shows the region after the leading edge and before the cross-points, where the droplet initiates its elongation. A 3D contour of the deformed droplet at the leading edge is highlighted.

eigenvector  $\mathbf{n}_1$  [Valdés et al., 2022]. The  $e_{\lambda,max}$  parameter can be used to classify the flow type present in any given region and link it with the dispersed phase's deformation. For instance,  $e_{\lambda,max} \approx 0.816$  corresponds to axisymmetric extensional flows,  $e_{\lambda,max} \approx 0.408$  to squeezing flows, and  $e_{\lambda,max} \approx 0.707$  to simple shear flows [Valdés et al., 2022].

In accordance with the computational results given by Liu et al. [2005, 2006], all three typical flows can be visualized in Figure 3. In particular, regions of low  $e_{\lambda,max}$  values can be readily identified as arrow-patterned contours in the  $y$ -direction in between crossbar rows, implying the dominant presence of squeezing flows occurring due to the X-shaped position of the crossbars [Liu et al., 2006]. Similarly, a mirrored pattern of high  $e_{\lambda,max}$  values (most effective extensional deformation) can be clearly observed in the middle section of the mixer which precedes (in the  $x$ -direction) a row of cross-points. This is in agreement with Liu et al. [2005] work who identified the droplet's stretching to take place in this region. Moreover, the velocity vectors and streamlines show that the flow is convergent and divergent at high and low  $e_{\lambda,max}$  values, which have been previously identified as natural features of extensional and squeezing flows, respectively [Liu et al., 2006]. This interplay between converging and diverging flows generates the characteristic recirculation regions shown around the crossbars.

Figure 4 shows the temporal evolution of a single droplet deforming at a cross-point, compared side-by-side against the experimental images and computationally generated data from a CFD-VOF model, as reported in Liu et al. [2005]. Qualitatively, an outstanding resemblance can be noted between the current study's simulation and the experimental data provided by Liu et al. [2005]. The full three-dimensional deformation mechanism of the droplet is closely copied by the tracking algorithm, unlike the VOF simulation which fails to capture subtle yet critical details such as the asymmetrical position of the daughter lobes generated after the collision with the cross-point ( $t = 500$  ms) or the slight in-



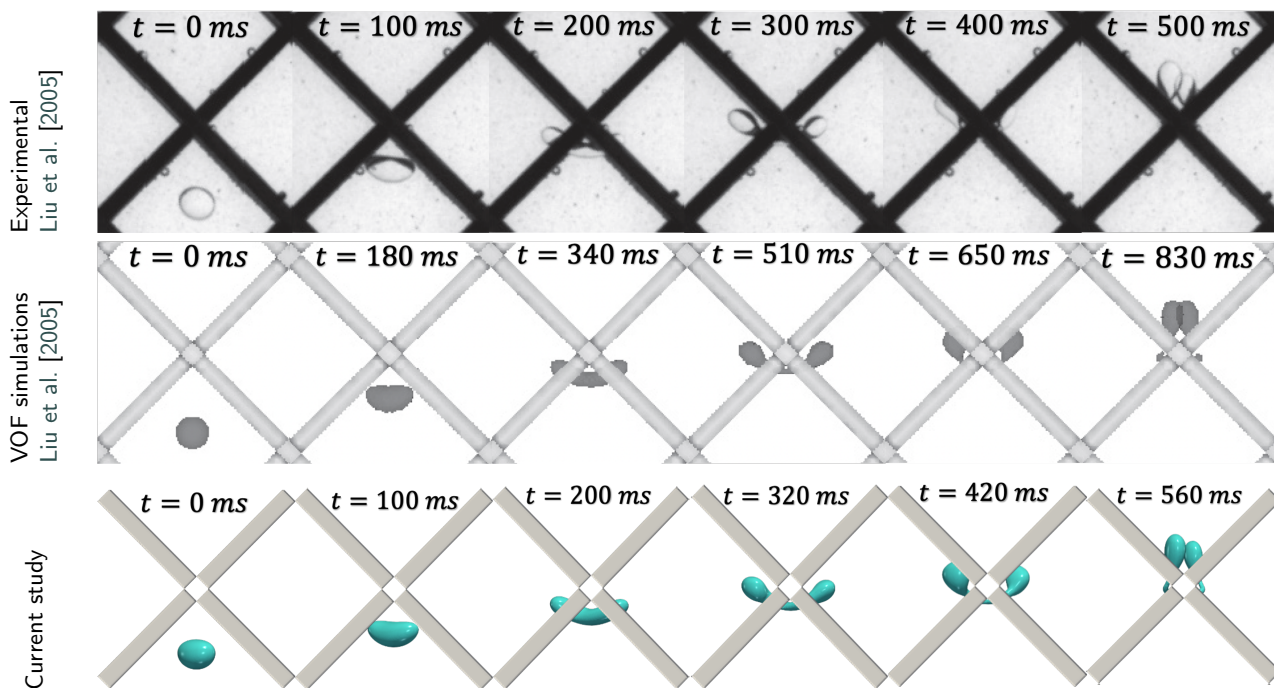


**Figure 4:** Temporal evolution of a single droplet undergoing deformation and breakup at a cross-point at  $Re = 1.2$  (bottom row), compared against the experimental (top row) and VOF-generated (middle row) images taken from Liu et al. [2005]

clination of the drop towards the left side of the cross-point during the initial stretching ( $t = 100$  ms and  $t = 200$  ms). Furthermore, a remarkable quantitative agreement between the experiments and the simulations performed in this work is achieved, given that the temporal scale of the deformation follows very closely the experimental times reported by Liu et al. [2005] (with deviations always under 20 ms except for the last snapshot). A considerable improvement in accuracy is obtained in this study when compared to the VOF calculations carried out by Liu et al. [2005], decreasing the average time deviations between snapshots from 69.7% to 4.73%, yielding a substantially closer time-frame to the experiments (60 ms deviation overall) compared to the VOF results (330ms deviation overall).

Finally, a mesh independence study similar to the one conducted by Constante-Amores et al. [2020] was carried out with the same case shown in Figure 4 to guarantee the independence of the results discussed in the upcoming sections from the grid's resolution. For this, three mesh sizes were examined ( $M_1$ ,  $M_2$ ,  $M_3$ ), and the shape and temporal evolution of the deforming drop were compared among them. The resolution of each of the grids tested is shown in the legend of Figure 5 and the respective cell volumes are as follow:  $M_1 \equiv 2.6 \times 10^{-11} \text{m}^3$ ,  $M_2 \equiv 3.3 \times 10^{-12} \text{m}^3$  (validation case shown in Figure 4) and  $M_3 \equiv 4.8 \times 10^{-13} \text{m}^3$ . From Figure 5, it is evident that the shape of the droplet barely changes between the two more refined grids tested, since an almost identical overlap can be observed in both the 2D and 3D contours. Furthermore, all grids maintain the same temporal evolution of the deformation, yielding a similar shape at

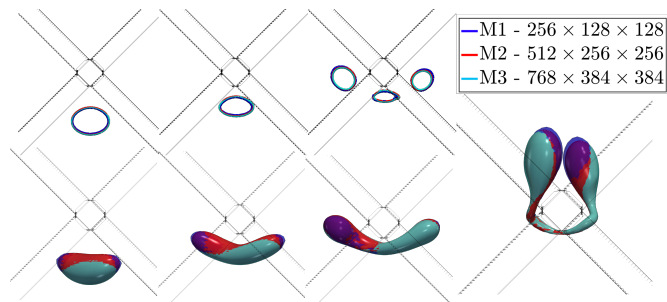


**Figure 5:** Grid independence study for the single drop breakup described in Figure 4 (from left to right  $t = 100$  s,  $t = 200$  s,  $t = 320$  s and  $t = 560$  s). Top and bottom rows show the 2D and 3D overlapped visualizations, respectively. Final shape of the droplet displayed in Figure 4 is given to the right.

each time established in Figure 4. The approximate cell volume used for the case-studies considered in this paper (refer to Figure 2) is on the order of  $V_{cell} \sim 10^{-14} \text{m}^3$ , based on the arguments explained previously (see Section 2.1). Considering the negligible variations observed between grids M1 through M3, there should be only minor differences with the higher resolution used for the results shown henceforth.

## 4. Results and discussion

This section is divided into two parts: the first one encompasses a deep dive into the physics behind droplet deformation and interfacial topological transitions which lead to breakup events, focusing on the isolated scenarios and then

tracing back to the more complex cases, whilst the second one discusses the performance of all inlet configurations through various metrics.

It is essential to highlight the fact that the capillary number  $Ca = \frac{\dot{\gamma} D_0 \mu_c}{2\sigma}$  calculated at the leading edge for the isolated scenarios is well above the critical capillary number  $Ca_{crit}$  expected in this region, as established in previous studies for relevant comparable scenarios. This implies that the stress imbalance acting on the incoming droplet(s) will most likely lead to a breakup event. Experiments [Grace, 1982] and computations [Bentley and Leal, 1986] on ideal two-dimensional (2D) extensional flows (i.e., hyperbolic shear fields generated on a four-roll device), have estimated  $Ca_{crit}$  values of approximately 0.22 and 0.16, respectively, for the viscosity ratio considered in this work ( $r_{vis} = 0.16$ ). Experimental  $Ca_{crit}$  values calculated based on the maximum droplet size obtained in similar SMX mixers in a laminar regime [Liu et al., 2005, Streiff et al., 1999] closely agree with the ideal extensional flows as expected ( $Ca_{crit} = 0.19$ – $0.24$  in Liu et al. [2005]), given the predominant presence of stretching stresses at the leading edge and cross-points. On the other hand,  $Ca$  in this study was estimated to be 2.5, calculating the shear rate at the leading edge ( $\dot{\gamma} = 7.5 \times (8u_{av}/D_p)$ ) as proposed by Liu et al. [2005].

Moreover, the  $r_{vis}$  values tested herein (0.1–1) correspond to a minimum in the critical shear required for breakup, both for rotational and extensional fields, as well as a minimum stable drop deformation before breakup, according to the experimental data provided by Grace [1982]. Therefore, the discussion provided in the upcoming subsection is not universal, and might not be fully replicable in cases with substantially different flow regimes or fluid properties, resulting in far apart ranges of  $r_{vis}$  or  $Ca_{crit}$ . In such different scenarios, droplets might have larger stable drop deformations or require higher shear stresses for breakage events to occur, as seen from some of the experiments carried out by Liu et al. [2005]. Despite this, the basics behind the deformation and breakage mechanics, which are innately linked to the geometrically-dependent internal flow dynamics, can be easily extrapolated to more realistic and complex cases (i.e., multiple drops) operating within a similar flow regime and range of  $r_{vis}$  values, or scenarios where the  $Ca$  and  $Ca_{crit}$  maintain a similar ratio as the one calculated in this paper.

#### 4.1. Deformation and breakup mechanisms

As depicted in Figure 6, the dispersion process taking place in the 2-element SMX studied here can be clearly divided into two distinct stages. The first one encompasses a three-dimensional (3D) elongational deformation of the drop(s) governed by the internal flow dynamics, which are inherently dependent on the mixer’s geometry, as well as by buoyant and viscous forces imposed by the carrier phase. Initially, the approaching drop(s) at the leading edge is stretched, twisted and folded in a V-shape, forking into two elongating necks, each with a leading bulbous head (see the first vignettes in Fig. 6). These heads will continue to divide into new necks as they collide with cross-points further down the

element, generating long ligaments and thin satellite threads before advancing into the second SMX element. This first stage features a steep increase in the dispersed phase’s interfacial area  $A/A_0$  as a result of the elongating necks and the flattening of the interface as it wraps around the crossbars, as captured in the red-shaded region in Figure 6. Little to no breakage events occur thus far.

The second stage consists of further stretching and thinning out of the necks and ligaments formed previously, following a similar deformation as in the first stage described above. The continued stretching leads to fragmentation events via numerous interfacial instabilities, giving birth to daughter droplets and other satellite structures. This stage comprises a noticeably lower and non-monotonic growth of the interfacial area (particularly for the single-drop case), ending in a pseudo-stabilization/ plateau region ( $t \approx 0.5s$ ), but with a rapid increase in the number of detached structures or “drops” (refer to the blue-shaded region in Figure 6). This stage is also characterized by the appearance of irregular peaks and troughs in the number of “drops” as the dispersion carries on, which represent the competition between breakup and coalescence events taking place. This rivalry is partly responsible for the erratic inflections noted in the interfacial area for the single-drop case in Fig. 6a. As more drops are injected into the mixer, the breakage events tend to overwhelm the coalescence, resulting in a more stable increase in area and number of drops, as seen for the 3-drop case in Fig. 6b.

Each stage spans a similar time frame ( $t_r \approx 0.25s$ ), which loosely corresponds to the residence time of a detached structure travelling across the SMX element. The exit region labelled in Figure 6 corresponds to a stabilization zone, where the leading section of the interface exits the second element and travels to the end of the computational domain, experiencing no further strain imposed by the mixer. Usually this stage is outside the scope of the mixing process. However, given the short length of the SMX studied here and the considerable amount of drops being generated in this region, it is worth analyzing the breakage modes occurring as a result of the stresses induced by the SMX.

##### 4.1.1. First stage

This stage of the dispersion has been documented experimentally and numerically in the work of Liu et al. [2005]. The isolated cases discussed herein capture faithfully the evolution of this step as described therein and seek to provide further insights into the relevant physical dynamics taking place. Figure 7 displays the temporal progression of the droplets’ deformation as they collide and stretch past the leading edge of the mixer. In particular, three of the most relevant and recurrent deformation modes are highlighted here, from which it is possible to elucidate the relationship between the geometry-induced internal flow dynamics and the interface’s shape transformation. In addition, these temporal instances can be traced back directly to the signature inflections seen in the  $A/A_0$  curves in Fig. 6, especially for the single-drop case in Fig. 6a. The first two snapshots in Fig. 7 (a) and (b)

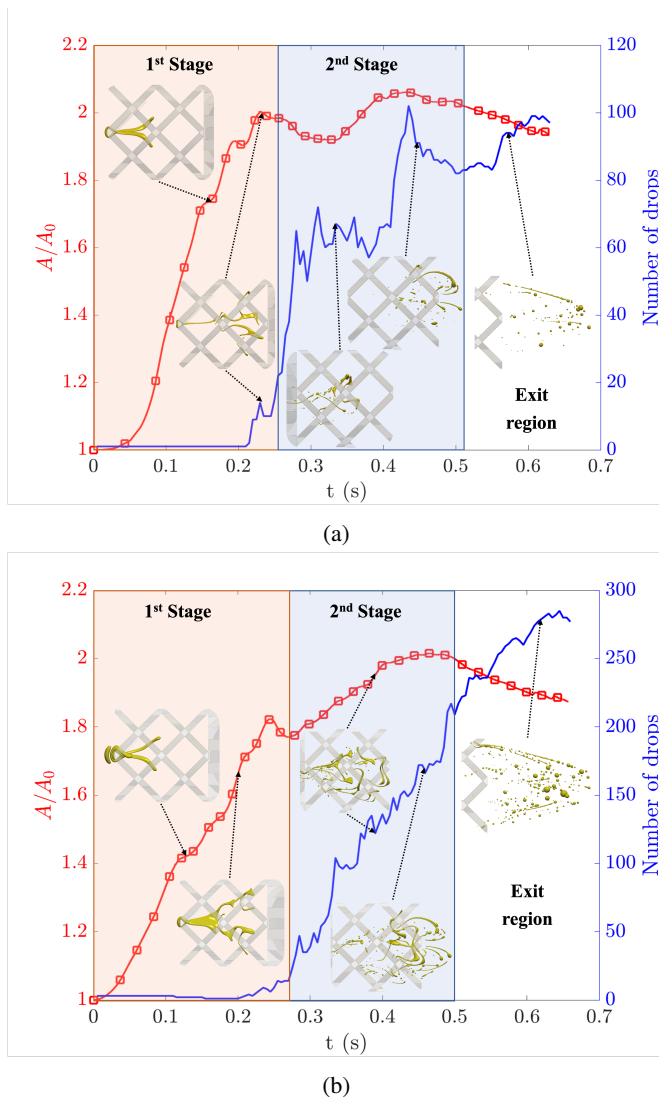


**Figure 6:** Temporal evolution of the dispersion dynamics observed for the isolated scenarios: a) 1-drop and, b) 3-drops cases, divided into two stages and an exit region at the mixer's outlet. Right axis displays the number of individual or detached interfacial structures (labelled as "drops" for simplicity), whilst the left axis displays the normalized interfacial area  $A/A_0$ .

correspond to a frequent solid-liquid interaction between the leading sections of the interface and the crossbars and cross-points: the neck's bulbous heads (or the drop itself at the leading edge) wrapping around the solids in a 3D V-shape, essentially creating two new necks. This forking event explains the slight shoulders in the  $A/A_0$  curves after  $t = 0.1s$ , given that the section of the interface that comes in contact with the solid is initially squeezed before the folding motion commences. More inflections are captured in the  $A/A_0$  curve in Fig. 6b due to additional wrapping events occurring further on, as shown at  $t = 0.2s$  in Fig. 7 (b).

The first snapshot in Fig. 7 shows the initial splitting of the incoming drops into two necks as they wrap around the leading edge, resulting in an initially flat V-shape as described by Liu et al. [2005]. Naturally, the presence of ad-

ditional drops slightly accelerate the elongation of the necks for the 3-drop case, but the shape adopted remains unchanged for both cases. The necks emerging from the drop(s) are caught by the high velocity corridors ( $u > 0.1$  m/s) formed in between crossbars but do not approach the high strain rate regions ( $\dot{\gamma} > 250$  s $^{-1}$ ) close to the bar itself, as gleaned from the 3D views and  $yz$  strain rate profiles in Figures 8 and 9 (a) (for more clarity, the high velocity corridors and high shear regions close to the bars can be identified from Fig. (2b)). At this moment, the stretching of the droplet's neck accelerates noticeably as its bulbous ends are pulled outwards through the gap between bars. Since the necks never pass through the vicinity of the bars (high strain rate zones) during the early stages of this process, the drop keeps being pulled from its ends mostly in one direction as clearly shown by the velocity vectors in Fig. 8 (a) and Fig. 9 (a), similar to the motion captured in Fig. 7 by the flow streamlines at times  $t = 0.205s$  and  $t = 0.2s$  for the 1 and 3 drop cases, respectively. In this way, opposing drag forces (mainly of viscous and buoyant nature) act homogeneously on the elongating necks. This hydrodynamic condition induces a mostly uniform shear stress distribution throughout the neck, similar to that depicted on the strain rate  $\dot{\gamma}$  profile at  $t = 0.205s$  in Fig.7 (a), in agreement with Liu et al. [2005]. Even though a less homogeneous distribution throughout the neck is obtained when dealing with additional droplets (see right-hand side of Fig. 7 (b)), the stresses at the unstable zones (leading and trailing sections of the neck's 2D projection) are still evenly distributed along the neck's radius. Very few pinching, high-strain regions are therefore formed throughout the necks during this stage of the dispersion, thus limiting the breakage events as discussed previously from Figure 6.

The characteristic 3D v-shape taken by the deforming interface during the folding mechanism can be tied to the intrinsically 3D spiral-type flow developed throughout the SMX element. When analyzed from a 2D  $xz$  view, different directions for the flow streamlines (parallel to the adjacent crossbar's orientation) can be noticed when moving radially across the element along the  $y$ -coordinate, as evidenced from the  $xz$  contours on the right-hand side of Fig. 7. This feature is noted to be a recurring pattern that alternates along the  $y$ -coordinate at each one of the corridors formed in-between crossbars in the  $z$  direction, as observed particularly from the 3D velocity vectors in Figs. 8 (a) and 9 (a,d). On the other hand, when seen from a 2D  $yz$  perspective (refer to profiles in Figs. 8 and 9 (b-c),(e-f)), these alternating flow currents give rise to recirculation zones near the crossbars, which are formed due to the interaction between the opposing flow directions. All these flow patterns come as a consequence of the x-shaped lattice arrangement of crossbars in the SMX, which when combined generate a distinctive 3D helical flow that dictates the evolution of the interface.

As depicted in the first snapshots of Fig. 7 and Figs. 8 and 9 (a), the necks initially travel through adjacent corridors with opposing flow directions, exhibiting the diverging V-shape mentioned earlier, until the leading bulbous heads are eventually caught in the recirculation zones close to the up-

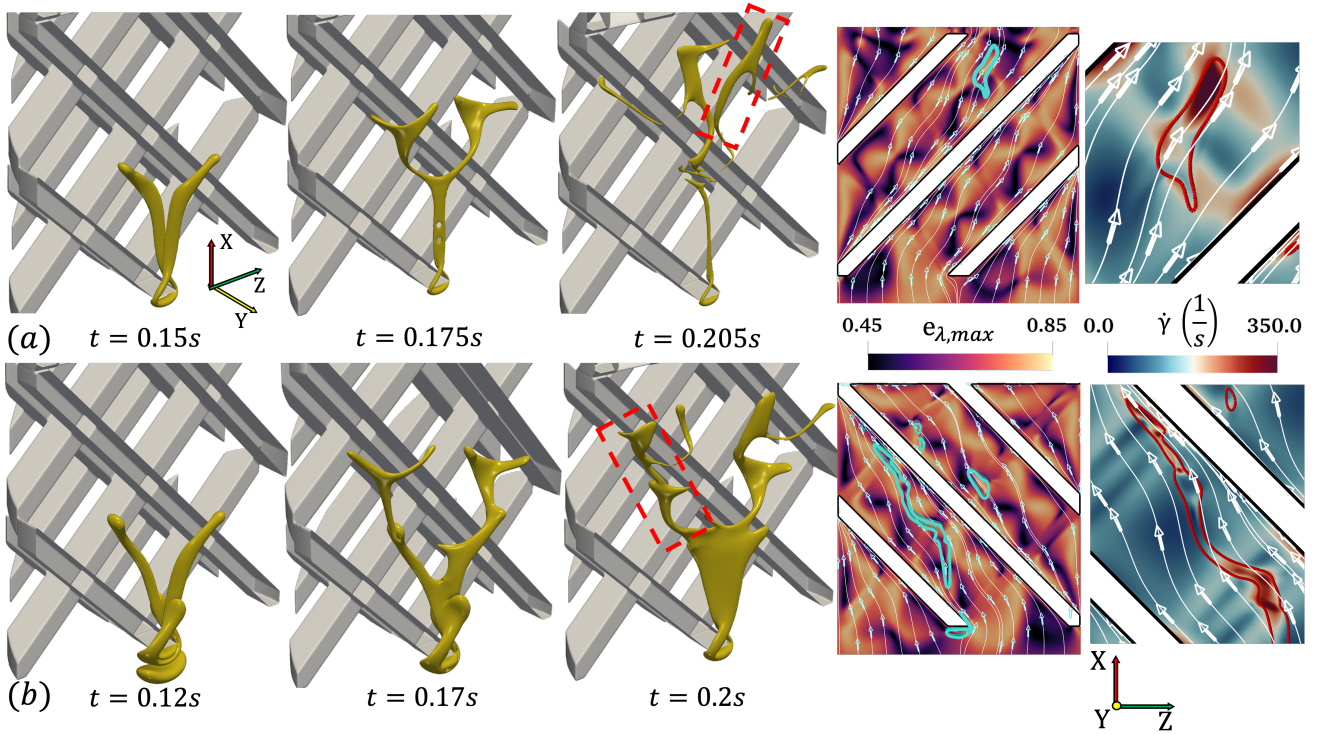


**Figure 7:** 3D visualization of the temporal evolution of the interface's deformation during the first stage of the dispersion process for: a) 1 drop, and b) 3-drop cases, respectively. Stretching efficiency  $e_{\lambda, max}$  and strain rate  $\dot{\gamma}$   $xz$  profiles with velocity streamlines for the final snapshot are given to the far right.

coming crossbars, triggering the wrapping motion at roughly  $t = 0.17s$  for both scenarios. Here, an inflection in the stretching direction of the interface occurs and a forking event takes place, spawning two new necks which will go on to enter opposing flow currents at the adjacent crossbar's corridors, thus stretching and diverging again in a V-shape (refer to Fig. 8 (d)). This explains why the elongating necks (especially for the single-drop case) experience several inflections in their curvature as they continue travelling through the element, resulting in a wavy S-shape when seen from a 2D  $xz$  perspective (refer to  $t = 0.205s$  in Fig. 7 (a)). The folding motion develops unevenly depending on the exact point of collision with the solid, exposing the enclosing interface to high shear stresses (see Fig. 8 (d)) and leading to the earliest breakage events registered in Fig. 6 in the first stage. This same morphology is also evident in the elongating neck located on the right-hand side for the 3-drop case at  $t = 0.2s$ , as shown in Fig. 7 (b).

A further discussion on this stage of the dispersion can be provided from the  $e_{\lambda, max}$  and flow topology  $Q$  profiles shown in Figures 8 and 9 (b,c) and (e-f). The flow field generated by the SMX grid configuration induces continuous regions of either converging stretching or diverging squeezing flows (high or low  $e_{\lambda, max}$  values, respectively [Liu et al., 2005, 2006]), which can be appreciated both in the  $yz$  cross-sections in Figs. 8 and 9 or the  $xz$  profiles given on the right-hand side of Figure 7. For instance, as previously discussed in subsection 3.2, arrow-shaped patterns of high and

low  $e_{\lambda, max}$  values can be identified along the  $y$ -coordinate, alternating in the  $z$  direction, as denoted by the  $yz$  profiles in Figs. 3, 8 and 9 (b). However, the stretching efficiency parameter does not always provide an unambiguous criterion for the prevailing flows dictating the dynamics taking place. For example, inside the corridors or close to the bars, the recirculation zones are commonly accompanied by fluctuating regions of high and low  $e_{\lambda, max}$  values, as noted from Figs. 8 and 9 (b,e). To circumvent this shortcoming, the flow topology parameter  $Q$  can be used to provide further key insights into other additional types of stresses present;  $Q$  is defined as the second invariant of the velocity gradient tensor  $\nabla u$  and is calculated as follows:

$$Q = \frac{D^2 - \Omega^2}{D^2 + \Omega^2}, \quad (19)$$

where  $D^2 = \mathbf{D} : \mathbf{D}$  and  $\Omega^2 = \mathbf{\Omega} : \mathbf{\Omega}$ , where  $\mathbf{\Omega}$  denotes the rate of rotation tensor [Soligo et al., 2020]. This criterion provides information on the dominant type of flow present in any given region, whether it is solely rotational ( $Q = -1$ ), shear ( $Q = 0$ ) or purely elongational ( $Q = 1$ ) [Soligo et al., 2020]. As expected, the continuous  $e_{\lambda, max}$  areas of either stretching or squeezing flows in the  $yz$  plane coincide with elongational flow regions of  $Q = 1$  (see Figs. 8 and 9 (b,c)). More importantly, a distinct and coherent combination of rotational ( $Q = -1$ ) and simple shear ( $Q = 0$ ) flows, consistent with the high strain-rate recirculating regions identified previously, can be established for the transitional zones in

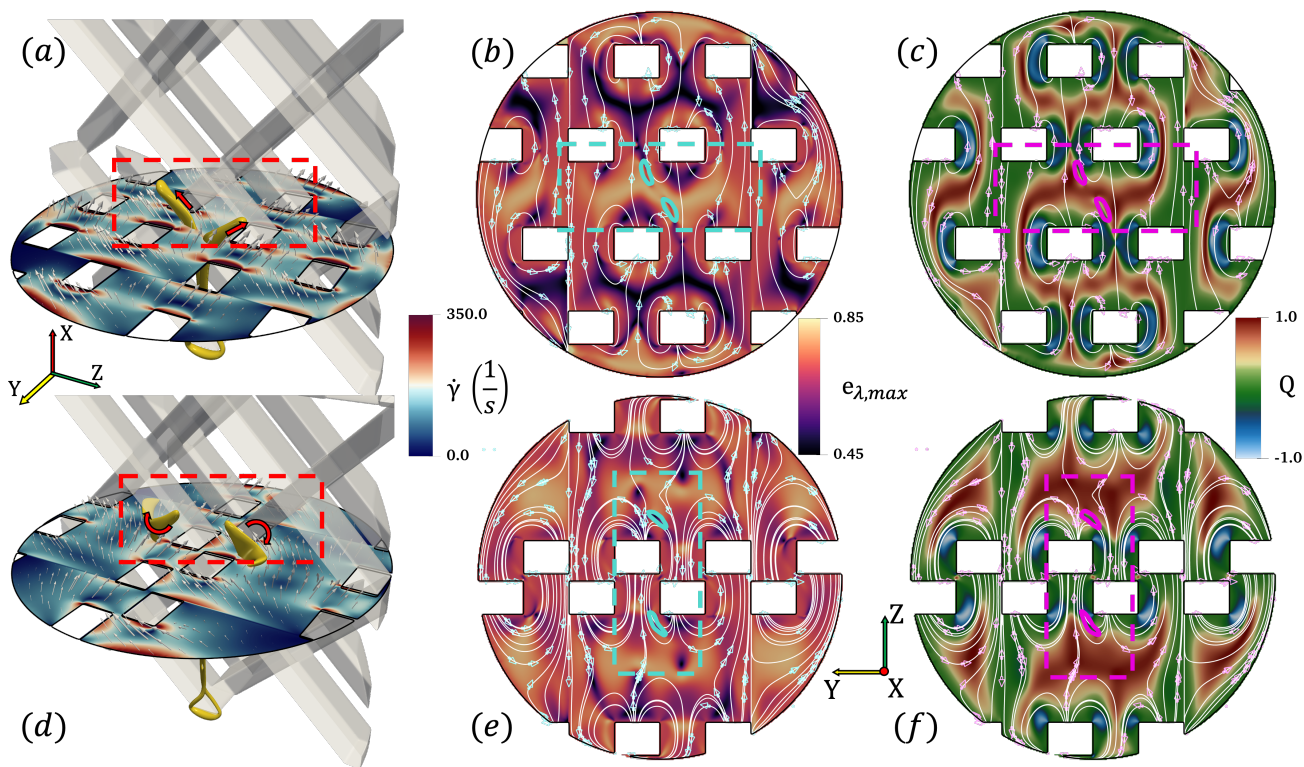


**Figure 8:** Hydrodynamic analysis of the deformation mechanics during the first stage of the dispersion: (a),(d) 3D view of the elongating interface (at  $t = 0.15s$  and  $0.175s$ , respectively) with velocity vectors set normal to a strain rate  $\dot{\gamma}$  coloured  $yz$  profile, (b),(e) 2D  $yz$  profile of the stretching efficiency  $e_{\lambda,max}$ , and (c),(f) 2D  $yz$  profile of the flow topology  $Q$ , both in the same  $x$ -coordinate and time as (b),(e) respectively.

the vicinity of the crossbars. These different sequences of dominating flow types dictate the initially steady deformation without breakup mechanism, as well as the characteristic enclosing evolution of the stretching necks around the crossbars and the early breakup events taking place before transitioning to the next stage.

At the highlighted areas in Figures 8 and 9 (b,c), the  $e_{\lambda,max}$  and  $Q$  values computed at the entrance of the gaps between crossbars, where the elongated necks travel at first, are generally  $e_{\lambda,max} \approx 0.8$  and  $Q \approx 1$ , indicating a dominant presence of converging elongational flows. Based on this, it can be argued that the neck's initially steady v-shape elongation without breakage occurs as a result of these converging flows driving the interface into the gaps between bars, stretching almost linearly thanks to the homogeneous presence of elongational stresses to which the interface is exposed, as verified from the  $Q$  profiles in Figs. 8 and 9 (c). This argument for the stretching without breaking dynamic is supported by the  $xz$   $e_{\lambda,max}$  profiles given in Fig. 7, which portray a nearly homogeneous extensional flow ( $e_{\lambda,max} \approx 0.8$ ) acting on unbroken elongating necks as they cross through the gaps between bars at a latter stage. Likewise, the folding and forking mechanism taking place in the proximity of the crossbars can be associated with the governing rotational

and shearing stresses acting on the interface. From Figs. 8 and 9 (f), it is evident that the section of the interface approaching the bars gets sucked into a region within the recirculation zone which is mostly comprised of rotational flows ( $Q = -1$ ), thus inducing the wrapping motion around the bar without any breakage. As the folding motion progresses, the interface gets thinned out due to its exposure to simple shear flows between the bars, denoted by  $Q = 0$  values as seen in Fig. 9 (f). This exposure will give rise to the first breakage events discussed previously.

In the 3-drop case considered herein, it is possible to observe the effects of early coalescence on the dynamics discussed so far. The most obvious one comes from the loss of symmetry (from a  $xz$  view) as the interface deforms, since one of the necks tends to continue spreading outwards (namely the left neck at  $t = 0.2s$  in Fig.7) instead of producing the wavy S-shape previously discussed. This results in longer filaments with a thicker radius as they journey into the second element. This may be attributed to several disruptions in the hydrodynamics examined at the crossbars' corridors due to the presence of additional droplets coalescing at the leading edge, thus altering the inertia carried by the expanding interface. It is possible to visualize the effect of these disruptions by comparing the  $yz$  profiles in Figs 8

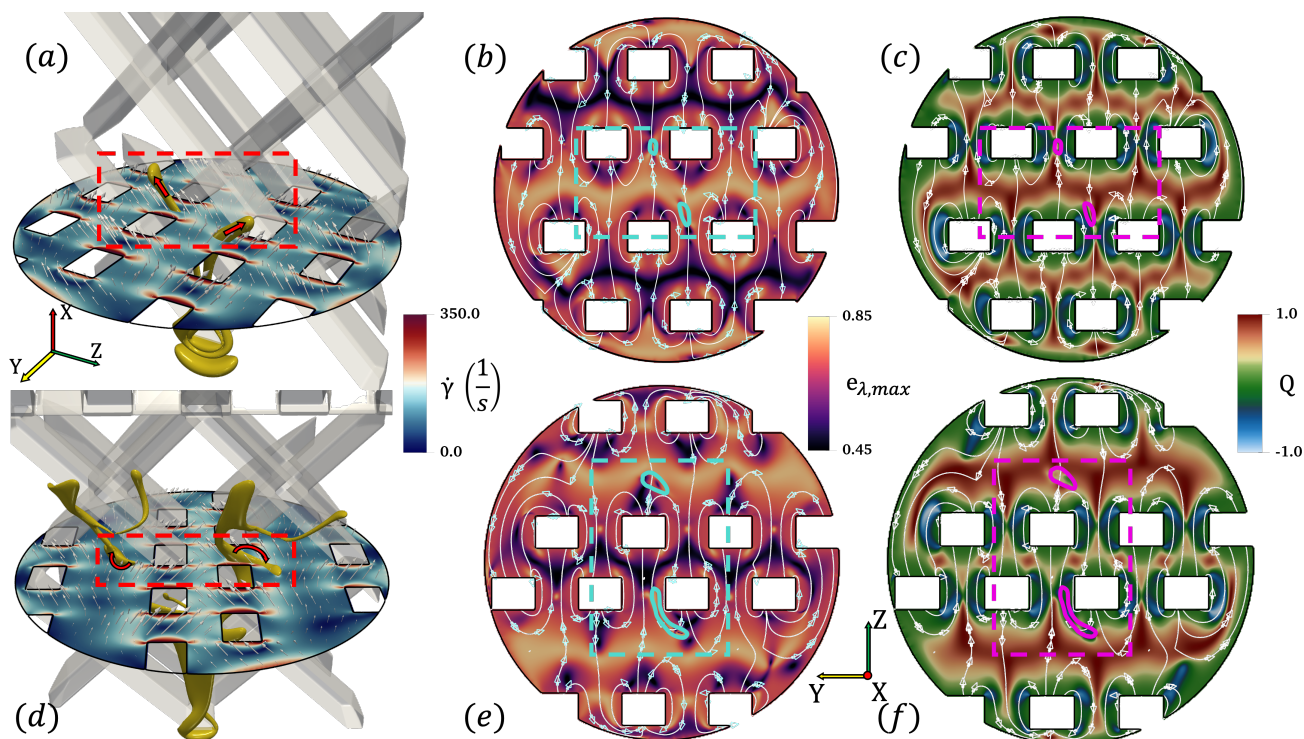


**Figure 9:** Same description as given in Figure 8 but for the 3-drop case at  $t = 0.12s$  and  $0.2s$  for (a-c) and (d-f), respectively.

and 9. For the 3-drop case in Fig. 9 (b,c), it is evident that the necks are not symmetrical, neither in shape nor position, since the upper neck's radius (left neck in the  $xz$  view) has been roughly thinned out by 50% and its position has been pushed further into the gap when compared to its equivalent in Fig. 8(b,c). By being thinner, the upper neck becomes more susceptible to buoyant and viscous forces as it keeps being stretched. Consequently, it gets pushed farther across the gap in the  $z$ -direction, preventing it from being caught by recirculation zones further ahead, thus delaying the folding motion explained before. The  $yz$   $e_{\lambda,max}$  and  $Q$  profiles in Figure 9 (e,f) support this analysis by showing the upper neck travelling through a mostly uniform extensional flow zone (high  $e_{\lambda,max}$  and  $Q$ ), whilst the bottom neck is caught in a rotational and shear dominated region close to the bars.

Another feature worth highlighting in the 3-drop case is the formation of additional ligaments and satellite threads through a similar wrapping and splitting dynamic as the one explored for the initial necks, primarily noticed in the left neck at  $t = 0.2s$  in Fig. 7. Since the initial collision between the leading bulbous head and the crossbar is delayed, the neck continues to stretch outwards, forming extra locations prone to fall into the recirculation zones, hence forming various new necks in the process. These extra ligaments will be directly responsible for the higher number of daughter drops generated during the second stage (refer to the blue-shaded areas in Figure 6), as will be discussed up next.

As addressed before, scattered breakup events during the first stage of the dispersion mostly occur at the cross-points

and bars. Here, emerging necks from the folding dynamic are exposed to high shear regions close to the solid, thus compromising the integrity of the interface and provoking the formation of a thinning and pinching region. This region originates from a stress imbalance occurring between the thicker and thinner spawning necks as they fold and get caught by opposing flow currents in the adjacent corridors to the bar. This mechanism will continue to arise across both elements during the second stage of the dispersion (geometrically-driven breakup defined up-next), as the remaining unbroken necks and long ligaments continue to get thinned out and disrupted by the shear dominating regions.

The deformation mechanisms described so far can be readily identified and extrapolated to the more complex and realistic scenarios studied in this paper, as exhibited in Figure 10, albeit with some variations (e.g., higher coalescence rates or larger disruption of the internal hydrodynamics). As captured in the left-hand side of Fig. 10a, numerous V-shaped elongating necks can be seen emerging from the leading edge of the mixer and wrapping again in the next series of cross-points midway through the first element, adhering to the mechanism detailed throughout this section. When analyzing individual instances, their behaviour is consistent with the hydrodynamic principles discussed earlier. For example, steadily stretching necks are commonly located in regions with dominating elongational flows (high  $e_{\lambda,max}$  and  $Q$ ) and low strain rate levels, whilst wrapping sections of the interface will be interacting with rotational and highly shearing flows in proximity to the bars ( $Q \leq 0$ ). Compa-

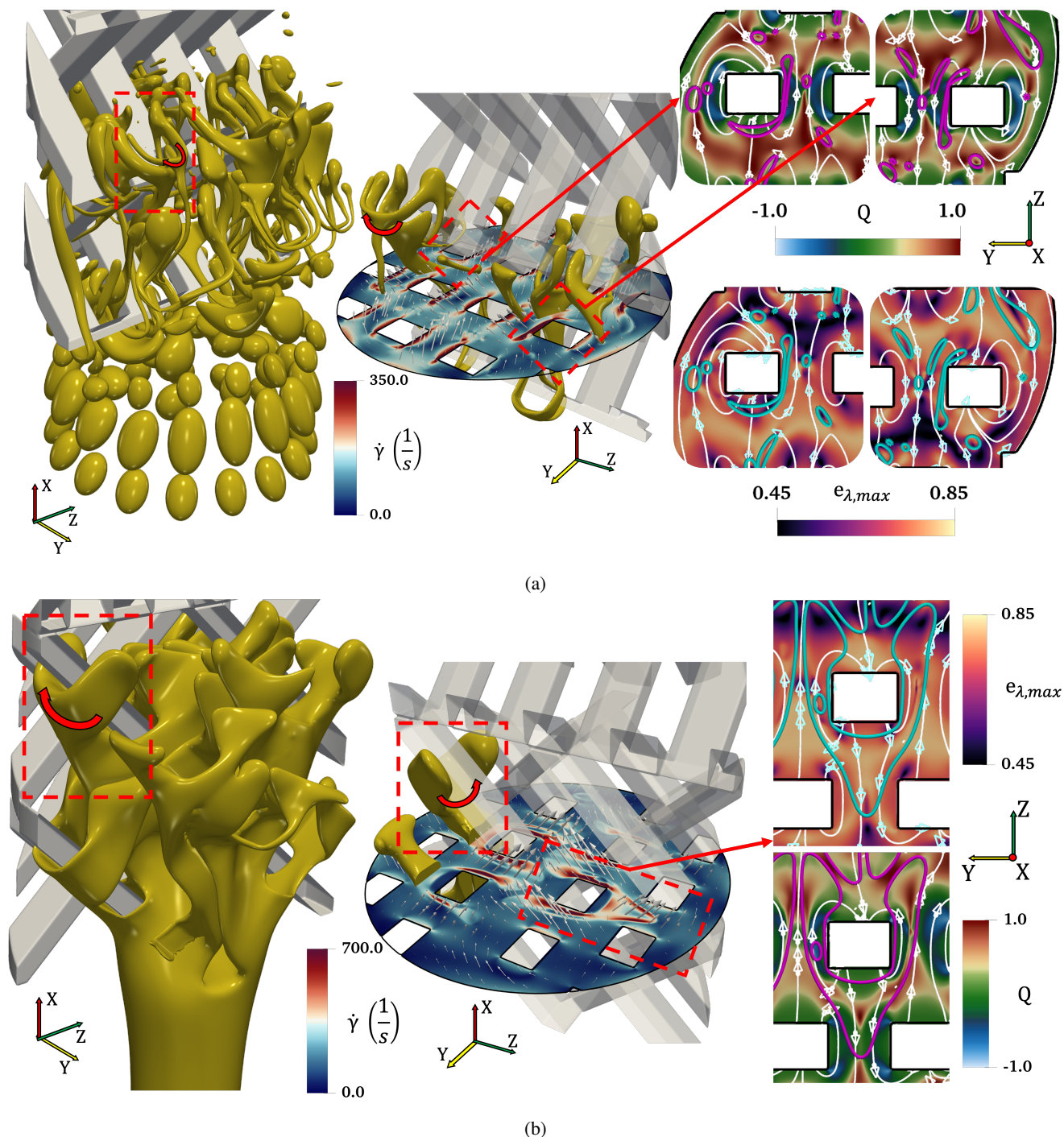


**Figure 10:** 3D view and hydrodynamic analysis of the deformation mechanics developing during the first stage of the dispersion for the complex scenarios: (a) Coarse pre-mixed inlet, (b) slow jet inlet. Similar to Figs. 8 and 9, three vignettes are presented from left to right: full 3D view, isolated 3D view with  $\dot{\gamma}$  profile and velocity vectors, and 2D  $yz$  inserts of the  $e_{\lambda,max}$  and  $Q$  parameters.

rable features can be spotted for the jet case in Fig. 10b, where the branches formed will have elongating sections at high  $e_{\lambda,max}$  and folding sections in the gaps between bars at  $Q \leq 0$ . The orientation of the spawning branches and necks can be directly related to the corridor's flow current to which they are exposed, always yielding diverging V-shaped

necks given the alternating nature of the currents. Slight differences between these and the isolated scenarios can be detected, such as the generation of several necks instead of only two during the wrapping mechanism, as seen throughout Fig. 10. Nonetheless, the trajectories and morphological evolution of these new necks can be predicted from the basic

concepts examined in this section.

#### 4.1.2. Second stage

The second stage of the dispersion comprises innumerable breakup mechanics taking place. Considering the intricacy of these mechanisms, even for the isolated scenarios, only two predominant dynamics will be examined and generalized: 1) hydrodynamically-driven breakup (type 1), mostly occurring from the fragmentation of elongated ligaments travelling through the second element, triggered by a myriad of interfacial instabilities; and 2) geometrically-driven breakup (type 2), occurring exclusively in the vicinity of the crossbars and cross-points, leading to the formation of a thinning and pinching region as explored in the previous subsection. These dynamics occur simultaneously, and can often be seen as a chain reaction process, where the type 2 breakup creates threads and ligaments which will later experience type 1 mechanics. It is important to mention that the grid resolution used in these simulations is not enough to provide an in-depth analysis of the hydrodynamic breakup physics (e.g., interaction of capillary waves, neck-pinching regime, etc.) as done in other works. However, this section attempts to shed light on some recognizable traits and invites further, more fundamental research on this aspect.

The most relevant hydrodynamically-driven mechanisms are shown in Fig. 11, where a multitude of stretching, retracting and fragmenting mechanics take place. These phenomena can be related to several previous studies dealing with liquid filaments [Schulkes, 1996, Lister and Stone, 1998, Notz and Basaran, 2004, Castrejón-Pita et al., 2012, Driessen et al., 2013, Castrejón-Pita et al., 2015, Wang et al., 2019], despite the fact that most consider liquid-air systems and neglect viscous drag effects or external inertial forces. As mentioned by Castrejón-Pita et al. [2012] and Wang et al. [2019], viscous drag from the surrounding fluid was deemed to be insignificant for filaments with radius smaller than  $R_0 < \mu_{air}/\rho\sigma$  (where  $\mu_{air} = \mu_c$  in this study). This criterion renders a  $R_0 \approx 1.8$  mm for the present work, comparable to the initial drop diameter  $D_0$ , implying that viscous drag effects will certainly play a major role. Considering this, and given the impossibility to provide a general sense of the relevant physical characteristics (e.g., aspect ratio  $\tilde{L}_0$ , Ohnesorge number  $Oh = \mu/\sqrt{\rho R_0 \sigma}$ ) for all filaments, specific cases in Fig. 11 will be addressed qualitatively and generalized for the rest of similar events happening.

Frequently, two distinctive ligament shapes can be identified during the second stage of the dispersion: asymmetric "dog-bone" shaped filaments with one or more minimum radius (see red and blue dotted regions in Fig. 11, respectively), and bulbous head and tail pairs (see green dotted region in Fig. 11). Other transient states can be identified such as irregular elongated columns or complex oscillating structures (comparable to those reported in Notz and Basaran [2004], Wang et al. [2019]), which in the end will evolve into dog-bone threads, bulbous heads and tails, or stable spherical drops, through a variety of break or no-break modes. The fate of all these states is mainly determined by the morphol-

ogy of the ligament (e.g., aspect ratio  $\tilde{L}_0$ , structural features and deformities) and the prevailing forces acting on them (e.g., external inertia or capillary vs. viscous given by  $Oh$ ) [Schulkes, 1996, Lister and Stone, 1998, Notz and Basaran, 2004, Castrejón-Pita et al., 2012, Driessen et al., 2013]. Early studies proposed well-defined thresholds in terms of  $Oh$  and  $\tilde{L}_0$  to determine the filament's fate. Nevertheless, recent studies have exposed a plethora of intermediate regimes existing in-between these boundaries [Castrejón-Pita et al., 2015, Wang et al., 2019]. Three scenarios can be summarized based on the cases observed in this study:

1. Viscosity-dominated, where no breakup events occur. Instead, ligaments retract through dog-bone shapes into stable spherical drops [Schulkes, 1996, Notz and Basaran, 2004, Castrejón-Pita et al., 2012]. This result is also shared by the "short-filament regime", delimited by a critical threshold  $\tilde{L}_{0,crit}$  [Castrejón-Pita et al., 2012, Wang et al., 2019].
2. Intermediate regime, where  $\tilde{L}_0$  is key in determining the fate of the ligament. At small and intermediate  $\tilde{L}_0$ , the filament undergoes a series of complex oscillations (i.e., capillary waves). The interactions of these fluctuations and the relative order of magnitude between the retraction and end-pinching characteristic times dictate the break or no-break modes occurring (wave-interaction regime) [Wang et al., 2019]. For short retraction times (smaller  $\tilde{L}_0$ ), oscillating filaments thicken at their ends and recoil into stable spheres, whereas for longer retraction times (larger  $\tilde{L}_0$ ), complex oscillating shapes lead to delayed breakup via end-pinching [Schulkes, 1996, Notz and Basaran, 2004, Castrejón-Pita et al., 2012, Wang et al., 2019]. At even larger  $\tilde{L}_0$ , breakup takes place via Rayleigh-Plateau instabilities, which are triggered by wave-like disturbances that have enough time to travel through the filament's surface [Driessen et al., 2013].
3. Capillary-dominated, where breakup will most likely occur via end-pinching, provided that  $\tilde{L}_0$  is sufficiently large [Notz and Basaran, 2004, Castrejón-Pita et al., 2012, Driessen et al., 2013, Wang et al., 2019]. In this regime, the pinch-off temporal scale is too short for surface disturbances to develop.

An example of a filament in the intermediate regime is shown to the right of Fig. 11, which at first travels with a bulbous head and tail morphology (not shown) before colliding with a cross-point, thus prompting the spread of interfacial instabilities along the ligament. Initially, capillary forces are not strong enough to overcome viscous forces, thus inhibiting the thinning of the bridge between the bulbous head and tail and precluding a pinch-off [Notz and Basaran, 2004]. However,  $\tilde{L}_0$  is sufficiently large in this case to provide a long enough retraction time for wave-like disturbances to develop, triggering Rayleigh-Plateau instabilities [Driessen et al., 2013]. The impact with the cross-point precipitates such instabilities, which in due course leads to the numerous



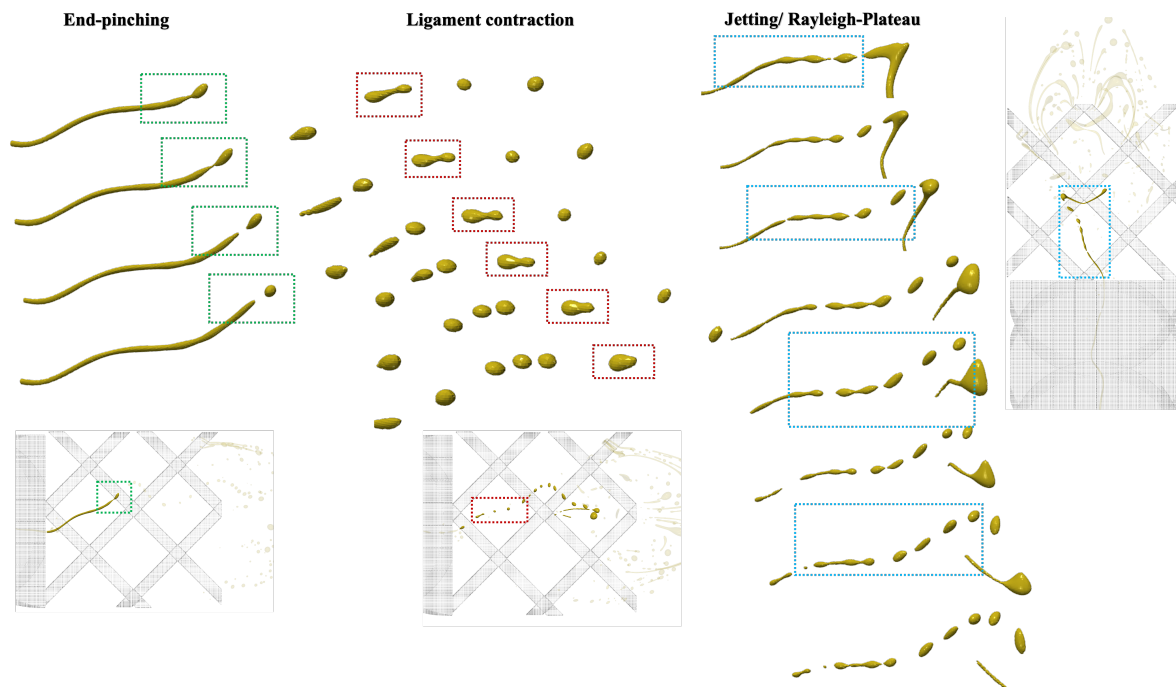


**Figure 11:** A myriad of ligament instabilities for the 3-drop scenario. In particular, the temporal evolution of three notable events: 1) Left, highlighted in green, droplet birth via end-pinchning mechanism from an elongating ligament, 2) Center, highlighted in red, dog-bone shaped ligament deforming and retracting into a stable sphere, and 3) Right, highlighted in blue, breakage events via Rayleigh-Plateau instabilities developing through the elongating ligament's surface, generating droplets in a jetting motion.

breakage events captured in Fig. 11. Most of the daughter threads formed early on continue behaving under the same regime by embracing a two-minima dog-bone shape and engaging in a succession of end-pinchning breakups, similar to those described by Lister and Stone [1998].  $\tilde{L}_0$  in this case is short enough to avoid wave-like perturbations to develop but long enough to yield comparable temporal scales for the retraction and pinch-off, thus inducing delayed breakup events [Wang et al., 2019, Castrejón-Pita et al., 2015].

On the other hand, viscosity and capillary dominated incidents are shown in the center and left of Fig. 11, respectively. The scenario shown in the centre of Fig. 11 depicts an initially unstable ligament (red dotted area) adopting a single minimum dog-bone shape, which undergoes an oscillating retracting motion and transitions into a stable spherical drop. As mentioned above, this occurs thanks to the very short retraction time associated with the ligament's small  $\tilde{L}_0$  [Schulkes, 1996, Notz and Basaran, 2004, Castrejón-Pita et al., 2012]. The case in the left panel of Fig. 11 shows a long ligament with a thinning neck between the head and tail. Capillary forces overcome viscous resistance in this case, resulting in a very short temporal scale for the pinch-off event, which prevents both surface disturbances to develop along the rest of the ligament and retracting motion pulling the bulbous head back to the rest of the filament.

The wave oscillations provoking Rayleigh-Plateau instabilities can be identified from the flow field present in the surroundings of the ligament. As noted in Fig. 12a, at the mo-

ment of fragmentation, a well-defined alternating pattern of  $Q = 0$  and  $Q = 1$  values is formed in the proximity of the ligament. This indicates a simultaneous interaction of successive rotational flows and shearing stresses coming from the perturbations propagating across the ligament's surface, ultimately leading to a Rayleigh-Plateau instability. A similar conclusion can be reached when replacing  $Q$  with the  $e_{\lambda,max}$  parameter, where predominantly squeezing flows close to the pinching regions and stretching flows near the lobes can be identified. A comparable relationship can be established by exploring the flow field present in the capillary-dominated end-pinchning mechanism discussed above from Fig. 11. As seen from Fig. 12b, mostly constant elongational flows at  $Q = 1$  are noted to the back of the bulbous head in proximity to where the tail is travelling. As seen to the left of Fig. 11, no major surface disturbances can be noticed along the filament's tail. In contrast, the thinning bridge where the pinch-off event unfolds comprises a sequence of rotational and shearing flows, akin to those observed for the Rayleigh-Plateau instabilities.

The higher count of long filaments formed during the first stage in the 3-drop case accounts for the higher number of daughter droplets generated in comparison to the 1-drop baseline case. This is mostly due to the recurrent breakup mechanism taking place for these ligaments, as discussed above. As seen from Fig. 11, a breakage via Rayleigh-Plateau instability naturally leads to the formation of multiple daughter droplets and satellite threads. Furthermore, the emerg-

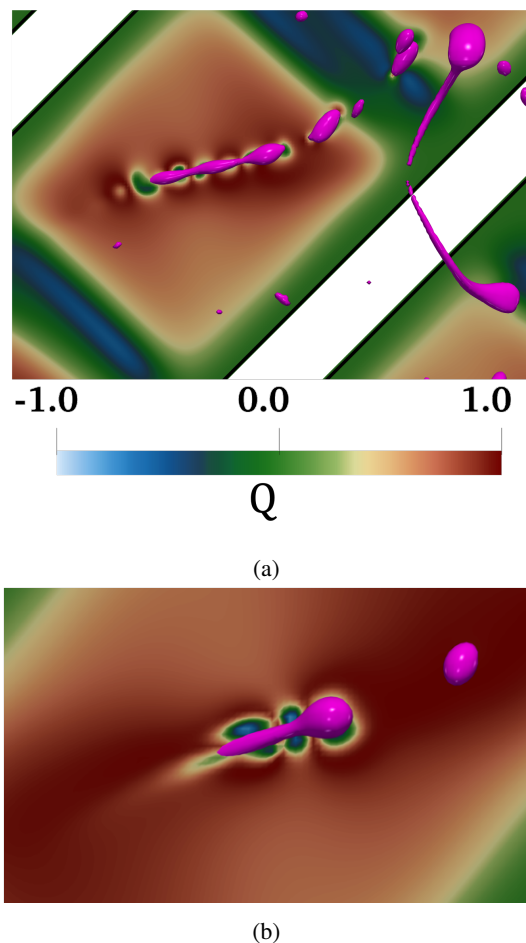


**Figure 12:** Flow topology  $Q$  profiles for: a) Breakup events via Rayleigh-Plateau instability, and b) breakup event via end-pinching, taken from the cases shown in Fig. 11.

ing threads were seen to commonly adopt shapes with multiple minimum radii suggesting a strong propensity for the formation of satellite droplets following the end-pinching of such threads [Lister and Stone, 1998]. In contrast, the shorter and sparser ligaments present in the baseline case usually adhered to end-pinching breakups at the bridge between the bulbous end and tail, resulting in far less satellite drops from each breaking event. The  $\tilde{L}_0$  for the tails usually is not enough to provide a long enough retraction time for further surface instabilities to spawn, thus eventually retracting into stable spheres. The majority of the daughter drops for the baseline case are produced via geometrically-driven breakup throughout both elements, in agreement with Liu et al. [2005] experimental images.

It is worth noting that a fair share of daughter droplets are also generated via geometry-driven breakage in the 3-drop case, and obtaining a higher drop count was expected. Nonetheless, as the mixer handles higher dispersed phase fractions, the majority of breakage events originate from fragmenting long ligaments due to interfacial instabilities, aided by external inertial forces from the flow. This comes as a consequence of early coalescence events as discussed earlier,

which enable early elongating necks to delay their exposure to high strain regions and enable the formation of more ligaments from folding dynamics.

#### 4.2. Comparative performance

The metrics selected to assess the performance of the SMX are: the normalized interfacial area  $A/A_0$ , the number of fully separated interfacial structures or "drops", and the DSD calculated at the moment where the first drop exits the computational domain. As seen from Figure 13a, the curves for the jet inlet morphology were offset from time 0, starting later at  $t = 0.04s$  and  $t = 0.08s$  for the jet with higher and lower inlet flowrate, respectively (refer to Table 2). This delay in time corresponds to the moment when the jet is about to collide with the leading edge of the first SMX element. Therefore, the initial interfacial area  $A_0$  is taken at this time for each jet respectively, thus neglecting the initial area growth occurring as a result of its injection, making it comparable to the other scenarios tested.

The first observation drawn from Figure 13 is the consistent two-stage dispersion process identified for the pre-mixed scenarios as for the isolated cases, exhibiting each stage within a comparable time frame albeit with a less obvious transition in terms of interfacial growth ( $A/A_0$ ). In fact, a separation between stages cannot be highlighted solely from Fig 13a given that the pre-mixed  $A/A_0$  curves reveal a less dramatic rise during the first stage of the dispersion ( $\sim 1.35-1.55A_0$  at  $t = 0.25s$ ) compared to nearly doubling for the baseline case. Furthermore, the curves continue to rise through the second stage all the way to  $t \sim 0.5s$ , with no major inflections or a distinct plateau section indicating a pseudo-stabilization of the interface's growth, as discussed earlier for the isolated scenarios. This results in a heavy overlap of stage one features (monotonic  $A/A_0$  growth) with the onset of the second stage, making both steps indistinguishable from Fig. 13a alone. This was expected given the particular set-up considered where droplets enter in equally-spaced batches rather than at random. Accordingly, as the first layer of droplets breaks at the exit of the first element, the trailing layers start to deform. Likewise, the lack of inflections in the  $A/A_0$  curves for the pre-mixed vs. the isolated scenarios comes from this same overlap between deforming and breaking events, resulting in a virtually smooth behavior overall. Still, the production of daughter droplets captured in Fig.13b at  $t \sim 0.2s$  heralds the onset of the second stage, akin to the behavior discussed earlier from Fig. 6b.

In regard to the jet cases in Fig. 13a, a substantially larger rise in the  $A/A_0$  curves is clearly seen relative to the drop-based scenarios. This stems naturally from the fact that the dispersed phase is injected continuously, whereas the other cases consider a finite amount of dispersed phase. By comparing the maximum slope attained at any given time for all  $A/A_0$  curves, it is evident that both jet cases exhibit the largest ones as expected, given the added inertia coming from the injection itself. Furthermore, the growth rates for both jet cases remain nearly unchanged for most of the dispersion process, unlike the drop-based scenarios where

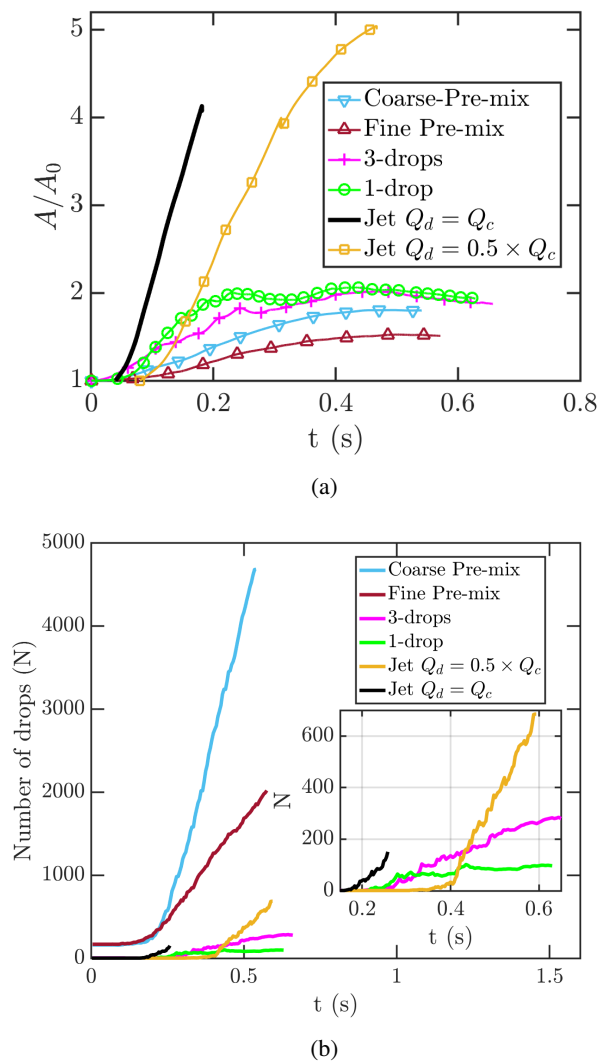


**Figure 13:** Comparative performance for all cases considered in this work: a) Temporal evolution of the normalized interfacial area, and b) temporal evolution of the number of detached interfacial structures (labelled as "drops" for simplicity). The starting point in a) for the jet simulations was set right before the interface collides with the mixer, thus neglecting the initial growth of the interface coming from the injection process.

there is either a distinct shift or a steady decrease in the  $A/A_0$  slope. This hints at a dominating presence of inertial over drag/viscous resistance forces, accounting for the variations discussed earlier from Fig. 10b in the deformation mechanics taking place. Additionally, it can be noticed that both slopes maintain a nearly proportional relationship against the injection flowrate  $Q_d$ , being approximately  $24.8 \text{ s}^{-1}$  and  $14.5 \text{ s}^{-1}$  for the faster and slower jet, respectively. This observation suggests that the interfacial rate of deformation is strongly governed by the dominant inertial forces related to the injection rather than by the continuous flow dynamics imposed by the geometry. This also explains why there is a considerably lower production of daughter droplets at a lower rate compared to the pre-mixed cases given the

shorter residence time to which the interface is exposed to high strain-rate regions and solid-fluid interactions. Although the onset of the breaking events (and thus the second stage) in Fig. 13b appears to be different for the jet cases, in reality it corresponds to the moment in time where the interface crosses the second SMX element, thus adhering to the same dispersion mechanism established for the isolated scenarios.

Another interesting result observed from Figure 13b is the disparity in the number of droplets obtained amongst the pre-mixed scenarios, despite having a relatively close development of the interfacial area (maximum  $A/A_0$  being 1.75 and 1.55 for the coarse and fine cases, respectively). The coarse pre-mix produced 4680 droplets compared to 2018 registered in the fine case, representing more than double the drop count recorded for the latter. The rate of droplet birth computed for both cases was noted to be rather stable, following a nearly linear tendency after the start of the second stage ( $t \sim 0.2$ s). The rate of birth for the coarser pre-mix compared to the fine case is nearly three times higher, being approximately 13 drops/ms compared to 4.5 drops/ms, assuming a linear trend. This implies that the mixer will perform more effectively, in terms of higher daughter droplet count and rate of birth, when handling initially larger drops, in agreement with Liu et al. [2005] findings. As reported therein, drops whose size lies within the same order of magnitude as the cross-bar gap tend to remain intact given the uniform shear stress distribution imparted to the drop, analogous to the discussion given in subsection 4.1.1. Likewise, very small droplets are less likely to break given their reduced probability of colliding with a high strain rate region and remaining long enough to absorb sufficient stress. Consequently, the performance of fine pre-mix case is worsened due to the higher count of small and gap-sized drops when compared against the coarse pre-mix.

A similar analysis can be drawn for the jet cases though it is worth mentioning that, due to computational feasibility, the fast jet simulation was stopped at the exit of the second element rather than the end of the domain; as a result, a direct comparison for the final number of drops between the two jet cases studied is not possible. When looking at the daughter droplet birth rate, a linear trend comparable to the pre-mixed set-ups can be noted for both jets. Moreover, a direct relationship between  $Q_d$  and the drop birth rate can also be established for both cases, computing 3.53 drops/ms and 1.74 drops/ms for the fast and slow jets, respectively, in agreement with the trends explored for the  $A/A_0$ . Despite the fast jet having a shorter residence time in the mixer, the added momentum from the injection is seen to improve the rate of drop birth by creating higher strain-rate levels close to the bars, thus facilitating breakage events to occur, as depicted in Fig. 10b. From this, a clear correlation can be established between the dispersion performance and the duration/intensity of the interfacial interaction with the high stress regions. Having a prolonged and/or more intense interaction between the interface and crossbars promotes the formation of ligaments (via type 1 mechanics) that will eventually break the interface via interfacial instabilities (type 2

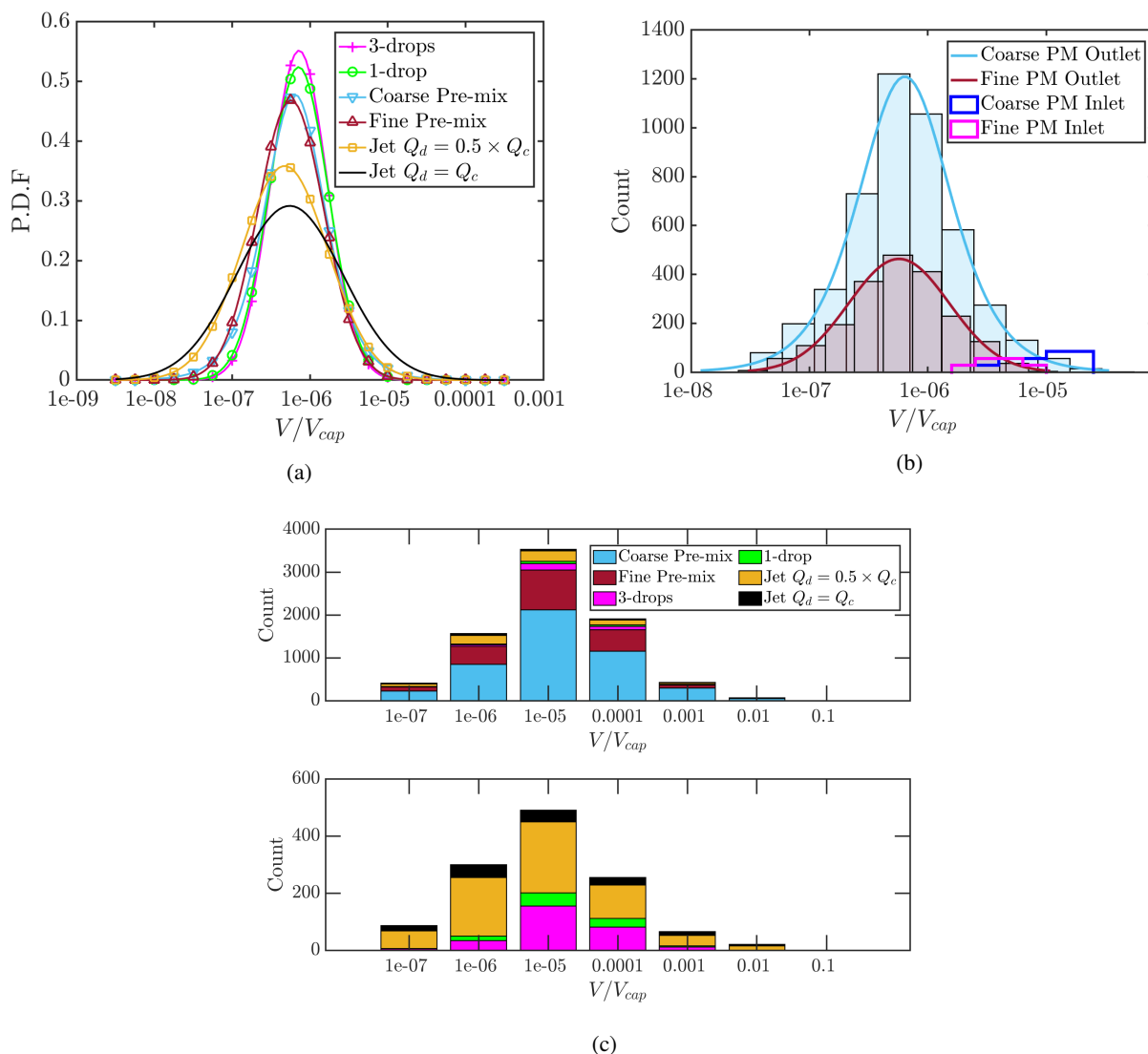


**Figure 14:** Comparative dimensionless droplet size distributions (DSDs) for all cases, taking as a reference the capillary volume  $V_c = 4\pi/3 \left( \sqrt{\sigma/g\Delta\rho} \right)^3$ . a) DSD histograms, b) Probability density functions (PDFs), and c) Comparative histograms and PDFs for the pre-mixed cases at the inlet and outlet.

mechanics), as explored in subsection 4.1.2. This also holds for the pre-mixed cases discussed above.

The number of droplets alone is not a representative metric of the SMX's dispersing performance, since numerous applications (e.g., cosmetics, food) heavily depend on the size distribution to achieve targeted end-product properties. For this reason, a statistical analysis on the outlet DSD was carried out for all cases simulated herein, as displayed in Fig. 14. Considering the inherent restrictions imposed by the grid's resolution when performing interface tracking analyses (e.g., non-physical/grid-dependent droplets), data were evaluated via quantile-quantile (Q-Q) and box plots to assess its structure and filter out points that differ significantly from the rest of the data-set. In this way, irrelevant large structures (e.g., unbroken main jet) or non-physical/numerically-

dependent tiny droplets are removed from the analysis. The filtered data-sets were fitted to a normal distribution, satisfying both Kolmogorov Smirnov (KS) and Anderson Darling (AD) normality tests with a level of significance of 0.05. The only exception comes from the coarse pre-mix case, which did not satisfy either test given that it features a pronounced asymmetric tail towards the larger end of the distribution (refer to Fig. 14b and 14c). Instead, a Logistic distribution was fitted to this data-set, in compliance with both KS and AD tests, providing a quasi-normal bell-shaped curve but with a slight skewness towards larger values. This deviation from normality comes as a consequence of initially injecting bigger droplets (see inlet DSD from Fig. 14b), which tend to spawn larger daughter droplets given that several of the emerging ligaments from stage 1 (refer to subsection 4.1.1)

will recoil into drops instead of breaking via interfacial instabilities.

Since some of the assumptions required to run an ANOVA (namely normality of the distributions and homoscedasticity) are not fulfilled in the data-sets studied here, a non-parametric Kruskal-Wallis test was performed instead. From this, a statistically significant difference was found between the medians of the jet vs. drop-based cases, although with some exceptions (i.e., significantly different medians between the fine and 3-drop cases, and no significant differences between the faster jet and the fine pre-mix). Nonetheless, the PDFs in Fig. 14a confirm an evident disparity between the jet vs. the drop-based DSDs. The former are visibly wider with broader tails, implying a larger variability of the drop sizes obtained. This observation is reinforced by computing and contrasting the skewness and kurtosis of the distributions. Both jet cases display a positive skewness (heavier right tail) of 0.855 and 0.603 for the fast and slow case, respectively, whilst most drop cases (except for the coarse pre-mix as expected) have a negative skewness, much closer to 0 (usually  $> -0.2$ ). In the same manner, both jet cases exhibit a much higher kurtosis (leptokurtic) compared to the drop-based setups, implying a heavier weight of the distribution's tails. This comes naturally due to the presence of very large detaching structures from the main jet co-existing with small daughter droplets appearing via fragmenting mechanics discussed in subsection 4.1.2. From Fig. 14a, and based on the skewness and kurtosis estimations, it is safe to assume that the DSD calculated for the fast jet case would have followed a much closer form to that of the slower jet if it was computed further, thus being just as different from all drop-based cases as the slower jet.

More importantly, the Kruskal Wallis analysis demonstrated that cases within the same type of set-up (i.e., isolated drops, multi-drop or jet) will not have significantly different DSDs between them. This suggests that, in the frame of the simulations performed here, modifying the operational parameters within a given configuration (e.g., different jet flowrate, different initial number of drops or drop sizes) does not have the same impact as completely changing the inlet configuration for the dispersed phase. The DSDs shown in Fig. 14b for the multi-drop configuration further support this idea, given that substantially different inlet DSDs will evolve into comparably shaped distributions, despite having a vastly different droplet count. Likewise, the pre-mixed PDFs in Fig. 14a closely overlap between them apart from slightly deviating at the tails. A similar observation can be made between the PDFs for the isolated drop set-up. This reasoning is in good agreement with previous literature, where it was been concluded that static mixers, and particularly multi-layered designs (i.e., SMX), will grant spatially uniform energy dissipation distribution with minimal dead zones [Valdés et al., 2022, Rama Rao et al., 2007, Lebaz and Sheibat-Othman, 2019]. Hence, changing the operational parameters in a constant set-up will affect the intensity of the energy but not the way it is being delivered to the dispersing fluid. On the contrary, different dispersed phase morphologies will have

a clear impact on the interaction between the fluid and the energy dissipated by the mixer.

## 5. Conclusions

In this study, a numerical analysis of the fundamental mechanisms governing a liquid-liquid dispersion process in a SMX static mixer was carried out. In particular, different inlet configurations were tested, aiming to isolate the underlying physics and extrapolate them to more realistic situations. Furthermore, the dispersion performance of the mixer, measured from the drop production and DSD, was evaluated and compared between the cases studied.

When exploring the fundamental physics of the isolated dispersion cases, a distinct two-stage process was identified. First, a complex elongational deformation with no breakup, dominated by the flow features imposed by the mixer's geometry, followed by the birth of daughter droplets occurring at the crossbars or via hydrodynamically-induced interfacial instabilities. The main highlight from this initial premise is its rather straightforward extrapolation to the more realistic and complex scenarios simulated herein. Both the multi-drop and jet cases adhered to a comparable two-stage process in the same time-span, and exhibited a remarkably similar shape evolution, albeit with slight variations due to various additional phenomena (e.g., higher coalescence events, dominating inertial forces). Furthermore, the complex cases (specially the coarse pre-mix case) displayed an overlap of stage 1 features during stage 2, where large enough daughter droplets in the second element would undergo the same deformation modes explored for stage 1. This may suggest a recurrent dispersing mechanism if more SMX elements are considered, where droplets keep deforming and breaking following the same two-step dynamics explored here.

The comparative performance analysis carried out demonstrated a clear relationship between the dispersed phase's inlet set-up and the dispersion metrics discussed previously. For a given inlet configuration, variations in key operational parameters (e.g., flowrate for jets, drop size for multi-drops) will affect the overall number of droplets produced at the end of the process. This occurs due to an external factor driving the breakage events, such as increased inertia from the jet's flow or simply having more dispersed phase present by having larger droplets. However, the DSD attained within a given set-up remains unchanged, given that the distribution of the energy dissipation and its delivery towards the dispersing fluid will remain consistent. In contrast, when the inlet configuration changes substantially, the interaction between the energy imparted by the mixer and the dispersed phase is altered, resulting in statistically significant deviations in the droplet sizes and the features of the distributions obtained. Future work is encouraged in terms of energy analysis and pressure drop for full-scale scenarios, given the clearly different energetic requirements each set-up carries.

The results and observations presented herein provide valuable insights into the governing physics of complex liquid-liquid dispersions in SMX mixers by offering an unprece-

mented level of detail on the underlying flow and interfacial dynamics taking place. This information can pave the way towards developing robust physics-informed design and optimization algorithms aiming to enhance the dispersing capabilities of the mixer. In addition, this work contributes to the current understanding of the possible performance related effects of selecting a given type of inlet configuration, and how to maximize a given dispersion metric from it.

### Acknowledgements

This work is supported by the Engineering and Physical Sciences Research Council, United Kingdom, through the EP-SRC MEMPHIS (EP/K003976/1) and PREMIERE (EP/T000414/1) Programme Grants. This work is also supported by the Colombian Ministry of Science, Technology and Innovation *MIN-CIENCIAS*, through a doctoral studentship for J.V. O.K.M. acknowledges funding from PETRONAS and the Royal Academy of Engineering for a Research Chair in Multiphase Fluid Dynamics. We also acknowledge the HPC facilities provided by the Research Computing Service (RCS) of Imperial College London. D.J. and J.C. acknowledge support through computing time at the Institut du Développement et des Ressources en Informatique Scientifique (IDRIS) of the Centre National de la Recherche Scientifique (CNRS), coordinated by GENCI (Grand Equipement National de Calcul Intensif) Grant 2022 A0122B06721. Simulations have been performed using code BLUE [Shin et al., 2017].

### References

- V. Abdolkarimi and H. Ganji. CFD modeling of two immiscible fluids mixing in a commercial scale static mixer. *Brazilian Journal of Chemical Engineering*, 31(4), 12 2014. ISSN 0104-6632. doi: 10.1590/0104-6632.20140314s00002857.
- Bengt Andersson, Ronnie Andersson, Love Håkansson, Mikael Mortensen, Rahman Sudiyo, and Berend Van Wachem. *Computational fluid dynamics for engineers*, volume 9781107018. 2011. ISBN 9781139093590. doi: 10.1017/CBO9781139093590.
- F. Azizi and A.M. Al Taweel. Turbulently flowing liquid-liquid dispersions. Part I: Drop breakage and coalescence. *Chemical Engineering Journal*, 166(2), 1 2011. ISSN 13858947. doi: 10.1016/j.cej.2010.11.050.
- A. Baumann, S.A.K. Jeelani, B. Hostenstein, P. Stössel, and E.J. Windhab. Flow regimes and drop break-up in SMX and packed bed static mixers. *Chemical Engineering Science*, 73, 5 2012. ISSN 00092509. doi: 10.1016/j.ces.2012.02.006.
- B. J. Bentley and L. G. Leal. An experimental investigation of drop deformation and breakup in steady, two-dimensional linear flows. *Journal of Fluid Mechanics*, 167(-1), 6 1986. ISSN 0022-1120. doi: 10.1017/S0022112086002811.
- Paul D. Berkman and Richard V. Calabrese. Dispersion of viscous liquids by turbulent flow in a static mixer. *AIChE Journal*, 1988. ISSN 15475905. doi: 10.1002/aic.690340409.
- Alfonso A. Castrejón-Pita, J. R. Castrejón-Pita, and I. M. Hutchings. Breakup of Liquid Filaments. *Physical Review Letters*, 108(7):074506, 2 2012. ISSN 0031-9007. doi: 10.1103/PhysRevLett.108.074506.
- José Rafael Castrejón-Pita, Alfonso Arturo Castrejón-Pita, Sumeet Suresh Thete, Krishnaraj Sambath, Ian M. Hutchings, John Hinch, John R. Lister, and Osman A. Basaran. Plethora of transitions during breakup of liquid filaments. *Proceedings of the National Academy of Sciences*, 112(15):4582-4587, 4 2015. ISSN 0027-8424. doi: 10.1073/pnas.1418541112.
- E. Chabanon, N. Sheibat-Othman, O. Mdere, J. P. Valour, S. Urbaniak, and F. Puel. Drop size distribution monitoring of oil-in-water emulsions in SMX+ static mixers: Effect of operating and geometrical conditions. *International Journal of Multiphase Flow*, 2017. ISSN 03019322. doi: 10.1016/j.ijmultiphaseflow.2017.03.001.
- Alexandre Joel Chorin. Numerical Solution of the Navier-Stokes Equations. *Mathematics of Computation*, 22(104), 10 1968. ISSN 00255718. doi: 10.2307/2004575.
- C.R. Constante-Amores, L. Kahouadji, A. Batchvarov, S. Shin, J. Chergui, D. Juric, and O.K. Matar. Direct numerical simulations of transient turbulent jets: vortex-interface interactions. *Journal of Fluid Mechanics*, 922:A6, 9 2021. ISSN 0022-1120. doi: 10.1017/jfm.2021.519.
- Cristian R. Constante-Amores, Lyes Kahouadji, Assen Batchvarov, Seungwon Shin, Jalel Chergui, Damir Juric, and Omar K. Matar. Dynamics of retracting surfactant-laden ligaments at intermediate Ohnesorge number. *Physical Review Fluids*, 5(8):084007, 8 2020. ISSN 2469-990X. doi: 10.1103/PhysRevFluids.5.084007.
- Mainak D. Das, Andrew N. Hrymak, and Malcolm H.I. Baird. Laminar liquid-liquid dispersion in the SMX static mixer. *Chemical Engineering Science*, 2013. ISSN 00092509. doi: 10.1016/j.ces.2013.06.047.
- Parichay K. Das, J. Legrand, P. Morançais, and G. Carnelle. Drop breakage model in static mixers at low and intermediate Reynolds number. *Chemical Engineering Science*, 2005. ISSN 00092509. doi: 10.1016/j.ces.2004.08.003.
- Theo Driessen, Roger Jeurissen, Herman Wijshoff, Federico Toschi, and Detlef Lohse. Stability of viscous long liquid filaments. *Physics of Fluids*, 25(6):062109, 6 2013. ISSN 1070-6631. doi: 10.1063/1.4811849.
- G. Forte, E. Brunazzi, and F. Alberini. Effect of residence time and energy dissipation on drop size distribution for the dispersion of oil in water using KMS and SMX+ static mixer. *Chemical Engineering Research and Design*, 2019. ISSN 02638762. doi: 10.1016/j.cherd.2019.06.021.
- Louis Fradette, B. Brocart, and P. A. Tanguy. Comparison of mixing technologies for the production of concentrated emulsions. *Chemical Engineering Research and Design*, 2007a. ISSN 02638762. doi: 10.1205/cherd06015.
- Louis Fradette, P. Tanguy, H. Z. Li, and L. Choplin. Liquid/liquid viscous dispersions with a SMX static mixer. *Chemical Engineering Research and Design*, 2007b. ISSN 02638762. doi: 10.1205/cherd06206.
- Akram Ghanem, Thierry Lemenand, Dominique Della Valle, and Hassan Peerhossaini. Static mixers: Mechanisms, applications, and characterization methods - A review. *Chemical Engineering Research and Design*, 92:205-228, 2014. ISSN 02638762. doi: 10.1016/j.cherd.2013.07.013.
- Jean Philippe Gingras, Louis Fradette, Philippe Tanguy, and Jacques Bousquet. Inline bitumen emulsification using static mixers. In *Industrial and Engineering Chemistry Research*, 2007. doi: 10.1021/ie0611913.
- Katuhiko Goda. A multistep technique with implicit difference schemes for calculating two- or three-dimensional cavity flows. *Journal of Computational Physics*, 30(1):76-95, 1 1979. ISSN 00219991. doi: 10.1016/0021-9991(79)90088-3.
- Harold P. Grace. Dispersion phenomena in high viscosity immiscible fluid systems and application of static mixers as dispersion devices in such systems. *Chemical Engineering Communications*, 1982. ISSN 15635201. doi: 10.1080/00986448208911047.
- M.M. Haddadi, S.H. Hosseini, D. Rashtchian, and G. Ahmadi. CFD modeling of immiscible liquids turbulent dispersion in Kenics static mixers: Focusing on droplet behavior. *Chinese Journal of Chemical Engineering*, 28(2), 2 2020. ISSN 10049541. doi: 10.1016/j.cjche.2019.07.020.
- Francis H. Harlow and J. Eddie Welch. Numerical Calculation of Time-Dependent Viscous Incompressible Flow of Fluid with Free Surface. *Physics of Fluids*, 8(12), 1965. ISSN 00319171. doi: 10.1063/1.1761178.
- S. Hirschberg, R. Koubek, F. Moser, and J. Schöck. An improvement of the Sulzer SMX™ static mixer significantly reducing the pressure drop. *Chemical Engineering Research and Design*, 2009. ISSN 02638762. doi: 10.1016/j.cherd.2008.12.021.
- F.P. Incropera, D. P. DeWitt, T. L. Bergman, and A. S. Lavine. Chapter 8: Internal Flow. In *Fundamentals of heat and mass transfer*, chapter 8. John Wiley & Sons, New York, sixth edition edition, 2007.
- Lyes Kahouadji, Emilia Nowak, Nina Kovalchuk, Jalel Chergui, Damir

- Juric, Seungwon Shin, Mark J. H. Simmons, Richard V. Craster, and Omar K. Matar. Simulation of immiscible liquid-liquid flows in complex microchannel geometries using a front-tracking scheme. *Microfluidics and Nanofluidics*, 22(11):126, 11 2018. ISSN 1613-4982. doi: 10.1007/s10404-018-2149-y.
- N. Kiss, G. Brenn, H. Pucher, J. Wieser, S. Scheler, H. Jennewein, D. Suzzi, and J. Khinast. Formation of O/W emulsions by static mixers for pharmaceutical applications. *Chemical Engineering Science*, 2011. ISSN 00092509. doi: 10.1016/j.ces.2011.06.065.
- Noureddine Lebaz and Nida Sheibat-Othman. A population balance model for the prediction of breakage of emulsion droplets in SMX+ static mixers. *Chemical Engineering Journal*, 2019. ISSN 13858947. doi: 10.1016/j.cej.2018.12.090.
- Sébastien Leclaire, David Vidal, Louis Fradette, and François Bertrand. Validation of the pressure drop-flow rate relationship predicted by lattice Boltzmann simulations for immiscible liquid-liquid flows through SMX static mixers. *Chemical Engineering Research and Design*, 153, 1 2020. ISSN 02638762. doi: 10.1016/j.cherd.2019.10.035.
- J. Legrand, P. Morançais, and G. Carnelle. Liquid-liquid dispersion in an SMX-Sulzer static mixer. *Chemical Engineering Research and Design*, 2001. ISSN 02638762. doi: 10.1205/02638760152721497.
- John R. Lister and Howard A. Stone. Capillary breakup of a viscous thread surrounded by another viscous fluid. *Physics of Fluids*, 10(11):2758-2764, 11 1998. ISSN 1070-6631. doi: 10.1063/1.869799.
- Shiping Liu, Andrew N. Hrymak, and Philip E. Wood. Drop breakup in an SMX static mixer in laminar flow. *Canadian Journal of Chemical Engineering*, 2005. ISSN 00084034. doi: 10.1002/cjce.5450830501.
- Shiping Liu, Andrew N. Hrymak, and Philip E. Wood. Design modifications to SMX static mixer for improving mixing. *AIChE Journal*, 2006. ISSN 0001-1541. doi: 10.1002/aic.10608.
- Emeline Lobry, Félicie Theron, Christophe Gourdon, Nathalie Le Sauze, Catherine Xuereb, and Thierry Lasuye. Turbulent liquid-liquid dispersion in SMV static mixer at high dispersed phase concentration. *Chemical Engineering Science*, 2011. ISSN 00092509. doi: 10.1016/j.ces.2011.06.073.
- Patrick K. Notz and Osman A. Basaran. Dynamics and breakup of a contracting liquid filament. *Journal of Fluid Mechanics*, 512, 8 2004. ISSN 0022-1120. doi: 10.1017/S0022112004009759.
- Charles S Peskin. Numerical analysis of blood flow in the heart. *Journal of Computational Physics*, 25(3), 11 1977. ISSN 00219991. doi: 10.1016/0021-9991(77)90100-0.
- Paulina Pianko-Oprych and Zdzisław Jaworski. CFD modelling of two-phase liquid-liquid flow in a SMX static mixer. *PJCT*, 11(3), 1 2009. ISSN 1899-4741. doi: 10.2478/v10026-009-0034-x.
- Paulina Pianko-Oprych and Zdzisław Jaworski. Prediction of liquid-liquid flow in an SMX static mixer using large eddy simulations. *Chemical Papers*, 64(2), 1 2010. ISSN 1336-9075. doi: 10.2478/s11696-009-0112-9.
- N. V. Rama Rao, M. H.I. Baird, A. N. Hrymak, and P. E. Wood. Dispersion of high-viscosity liquid-liquid systems by flow through SMX static mixer elements. *Chemical Engineering Science*, 2007. ISSN 00092509. doi: 10.1016/j.ces.2007.08.070.
- Damien Rauline, Philippe A. Tanguy, Jean-Marc Le Blévec, and Jacques Bousquet. Numerical investigation of the performance of several static mixers. *The Canadian Journal of Chemical Engineering*, 76(3), 6 1998. ISSN 00084034. doi: 10.1002/cjce.5450760325.
- R. M. S. M. Schulkes. The contraction of liquid filaments. *Journal of Fluid Mechanics*, 309:277-300, 2 1996. ISSN 0022-1120. doi: 10.1017/S0022112096001632.
- Seungwon Shin. Computation of the curvature field in numerical simulation of multiphase flow. *Journal of Computational Physics*, 222(2), 3 2007. ISSN 00219991. doi: 10.1016/j.jcp.2006.08.009.
- Seungwon Shin and Damir Juric. High order level contour reconstruction method. *Journal of Mechanical Science and Technology*, 21(2), 2 2007. ISSN 1738-494X. doi: 10.1007/BF02916292.
- Seungwon Shin and Damir Juric. A hybrid interface method for three-dimensional multiphase flows based on front tracking and level set techniques. *International Journal for Numerical Methods in Fluids*, 60(7), 7 2009a. ISSN 02712091. doi: 10.1002/flid.1912.
- Seungwon Shin and Damir Juric. Simulation of droplet impact on a solid surface using the level contour reconstruction method. *Journal of Mechanical Science and Technology*, 23(9), 9 2009b. ISSN 1738-494X. doi: 10.1007/s12206-009-0621-z.
- Seungwon Shin, S.I. Abdel-Khalik, Virginie Daru, and Damir Juric. Accurate representation of surface tension using the level contour reconstruction method. *Journal of Computational Physics*, 203(2), 3 2005. ISSN 00219991. doi: 10.1016/j.jcp.2004.09.003.
- Seungwon Shin, Jalel Chergui, and Damir Juric. A solver for massively parallel direct numerical simulation of three-dimensional multiphase flows. *Journal of Mechanical Science and Technology*, 31(4), 4 2017. ISSN 1738-494X. doi: 10.1007/s12206-017-0322-y.
- Seungwon Shin, Jalel Chergui, Damir Juric, Lyes Kahouadji, Omar K. Matar, and Richard V. Craster. A hybrid interface tracking - level set technique for multiphase flow with soluble surfactant. *Journal of Computational Physics*, 359:409-435, 4 2018. ISSN 00219991. doi: 10.1016/j.jcp.2018.01.010.
- Chi-Wang Shu and Stanley Osher. Efficient implementation of essentially non-oscillatory shock-capturing schemes, II. *Journal of Computational Physics*, 83(1):32-78, 7 1989. ISSN 00219991. doi: 10.1016/0021-9991(89)90222-2.
- Giovanni Soligo, Alessio Roccon, and Alfredo Soldati. Effect of surfactant-laden droplets on turbulent flow topology. *Physical Review Fluids*, 5(7):073606, 7 2020. ISSN 2469-990X. doi: 10.1103/PhysRevFluids.5.073606.
- F.A. Streiff, S.A. Jaffer, and G. Schneider. The Design and Application of Static Mixer Technology. In *Third International Symposium on Mixing in Industrial Processes*, pages 107-114, Osaka, 1999.
- Mark Sussman, Emad Fatemi, Peter Smereka, and Stanley Osher. An improved level set method for incompressible two-phase flows. *Computers & Fluids*, 27(5-6):663-680, 6 1998. ISSN 00457930. doi: 10.1016/S0045-7930(97)00053-4.
- R. K. Thakur, Ch Vial, K. D.P. Nigam, E. B. Nauman, and G. Djelveh. Static mixers in the process industries - a review. *Chemical Engineering Research and Design*, 81(7):787-826, 2003. ISSN 02638762. doi: 10.1205/026387603322302968.
- F. Theron and N. Le Sauze. Comparison between three static mixers for emulsification in turbulent flow. *International Journal of Multiphase Flow*, 37:488-500, 2011. ISSN 03019322. doi: 10.1016/j.ijmultiphaseflow.2011.01.004.
- Félicie Theron, Nathalie Le Sauze, and Alain Ricard. Turbulent liquid-liquid dispersion in sulzer SMX mixer. *Industrial and Engineering Chemistry Research*, 2010. ISSN 08885885. doi: 10.1021/ie900090d.
- P.G. Tucker. *Unsteady Computational Fluid Dynamics in Aeronautics*, volume 104. Springer Netherlands, Dordrecht, 2014. ISBN 978-94-007-7048-5. doi: 10.1007/978-94-007-7049-2.
- Juan P. Valdés, Lyes Kahouadji, and Omar K. Matar. Current advances in liquid-liquid mixing in static mixers: A review. *Chemical Engineering Research and Design*, 177, 1 2022. ISSN 02638762. doi: 10.1016/j.cherd.2021.11.016.
- M. P. Vasilev and R. Sh Abiev. Intensity and efficiency of droplet dispersion: Pulsating flow type apparatus vs. static mixers. *Chemical Engineering Research and Design*, 2018a. ISSN 02638762. doi: 10.1016/j.cherd.2018.07.029.
- M. P. Vasilev and R. Sh Abiev. Turbulent droplets dispersion in a pulsating flow type apparatus - New type of static disperser. *Chemical Engineering Journal*, 2018b. ISSN 13858947. doi: 10.1016/j.cej.2018.05.104.
- Alexander Vikhansky. CFD modelling of turbulent liquid-liquid dispersion in a static mixer. *Chemical Engineering and Processing - Process Intensification*, 149, 3 2020. ISSN 02552701. doi: 10.1016/j.ccep.2020.107840.
- F. Wang, F. P. Contò, N. Naz, J. R. Castrejón-Pita, A. A. Castrejón-Pita, C. G. Bailey, W. Wang, J. J. Feng, and Y. Sui. A fate-alternating transitional regime in contracting liquid filaments. *Journal of Fluid Mechanics*, 860:640-653, 2 2019. ISSN 0022-1120. doi: 10.1017/jfm.2018.855.